



**HAL**  
open science

## The WSRT ZoA Perseus-Pisces filament wide-field H I imaging survey - I. H I catalogue and atlas

M. Ramatsoku, M. A. W. Verheijen, R. C. Kraan-Korteweg, G. I. G. Józsa, A. C. Schröder, T. H. Jarrett, E. C. Elson, W. van Driel, W. J. G. de Blok, P. A. Henning

### ► To cite this version:

M. Ramatsoku, M. A. W. Verheijen, R. C. Kraan-Korteweg, G. I. G. Józsa, A. C. Schröder, et al.. The WSRT ZoA Perseus-Pisces filament wide-field H I imaging survey - I. H I catalogue and atlas. Monthly Notices of the Royal Astronomical Society, 2016, 460, pp.923-941. 10.1093/mnras/stw968 . insu-03720972

**HAL Id: insu-03720972**

**<https://insu.hal.science/insu-03720972>**

Submitted on 12 Jul 2022

**HAL** is a multi-disciplinary open access archive for the deposit and dissemination of scientific research documents, whether they are published or not. The documents may come from teaching and research institutions in France or abroad, or from public or private research centers.

L'archive ouverte pluridisciplinaire **HAL**, est destinée au dépôt et à la diffusion de documents scientifiques de niveau recherche, publiés ou non, émanant des établissements d'enseignement et de recherche français ou étrangers, des laboratoires publics ou privés.

# The WSRT ZoA Perseus-Pisces filament wide-field H I imaging survey – I. H I catalogue and atlas

M. Ramatsoku,<sup>1,2,3★</sup> M. A. W. Verheijen,<sup>1,4★</sup> R. C. Kraan-Korteweg,<sup>2★</sup> G. I. G. Józsa,<sup>5</sup>  
A. C. Schröder,<sup>6</sup> T. H. Jarrett,<sup>2</sup> E. C. Elson,<sup>2</sup> W. van Driel,<sup>7</sup> W. J. G. de Blok<sup>1,2,3</sup>  
and P. A. Henning<sup>8</sup>

<sup>1</sup>Kapteyn Astronomical Institute, University of Groningen, Landleven 12, NL-9747 AV Groningen, The Netherlands

<sup>2</sup>Astrophysics, Cosmology and Gravity Centre (ACGC), Department of Astronomy, University of Cape Town, Private Bag X3, Rondebosch 7701, South Africa

<sup>3</sup>ASTRON, Netherlands Institute for Radio Astronomy, Postbus 2, NL-7990 AA Dwingeloo, the Netherlands

<sup>4</sup>Adjunct Faculty, National Centre for Radio Astrophysics, TIFR, Ganeshkhind, Pune 411007, India

<sup>5</sup>SKA South Africa, Radio Astronomy Research Group, 3rd Floor, The Park, Park Road, Pinelands 7405, South Africa

<sup>6</sup>South African Astronomical Observatory (SAAO), PO Box 9, 7935 Observatory, Cape Town, South Africa

<sup>7</sup>GEPI, Observatoire de Paris, CNRS, Université Paris Diderot, 5 place Jules Janssen, F-92190 Meudon, France

<sup>8</sup>Department of Physics and Astronomy, University of New Mexico, 1919 Lomas Blvd. NE, MSC07 4220, Albuquerque NM 87131-0001, USA

Accepted 2016 April 21. Received 2016 April 21; in original form 2015 November 24

## ABSTRACT

We present results of a blind 21cm H I-line imaging survey of a galaxy overdensity located behind the Milky Way at  $\ell, b \approx 160^\circ, 0^\circ.5$ . The overdensity corresponds to a zone-of-avoidance crossing of the Perseus-Pisces Supercluster filament. Although it is known that this filament contains an X-ray galaxy cluster (3C 129) hosting two strong radio galaxies, little is known about galaxies associated with this potentially rich cluster because of the high Galactic dust extinction. We mapped a sky area of  $\sim 9.6 \text{ deg}^2$  using the Westerbork Synthesis Radio Telescope in a hexagonal mosaic of 35 pointings observed for 12 h each, in the radial velocity range  $cz = 2400\text{--}16\,600 \text{ km s}^{-1}$ . The survey has a sensitivity of  $0.36 \text{ mJy beam}^{-1} \text{ rms}$  at a velocity resolution of  $16.5 \text{ km s}^{-1}$ . We detected 211 galaxies, 62 per cent of which have a near-infrared counterpart in the UKIDSS Galactic Plane Survey. We present a catalogue of the H I properties and an H I atlas containing total intensity maps, position–velocity diagrams, global H I profiles and UKIDSS counterpart images. For the resolved galaxies we also present H I velocity fields and radial H I surface density profiles. A brief analysis of the structures outlined by these galaxies finds that 87 of them lie at the distance of the Perseus-Pisces Supercluster ( $cz \sim 4000\text{--}8000 \text{ km s}^{-1}$ ) and seem to form part of the 3C 129 cluster. Further 72 detections trace an overdensity at a velocity of  $cz \approx 10\,000 \text{ km s}^{-1}$  and seem to coincide with a structure predicted from mass density reconstructions in the first 2MASS Redshift Survey.

**Key words:** atlases – catalogues – surveys – galaxies: clusters: general – radio lines: galaxies.

## 1 INTRODUCTION

Major steps forward have been achieved in mapping the large-scale distribution of galaxies forming the Cosmic Web, thanks to dedicated wide-field (on-sky), deep (in terms of redshift) galaxy redshift surveys such as the 2dF Galaxy Redshift Survey (2dFGRS; Colless et al. 2001), the 2MASS Redshift Survey (2MRS, Huchra et al. 2012), the Sloan Digital Sky Survey (SDSS; Eisenstein et al. 2011) and the 6dF Galaxy Survey (6dFGS; Jones et al. 2004). The largest areal coverage is provided by the 2MRS with 44 000

galaxies. It is based on the brightest objects in the near-infrared 2MASS Extended Source Catalogue (2MASX; Jarrett et al. 2000) and has a relatively low median velocity of  $cz_{\text{med}} = 9000 \text{ km s}^{-1}$ . A version slightly deeper in velocity ( $cz_{\text{med}} = 15\,000 \text{ km s}^{-1}$ ) is achieved through a combination of the 2MRS, SDSS and 6dFGS catalogues into the 2M++ galaxy compilation by Lavaux & Hudson (2011), however, it is not homogenous in sky coverage. Bilicki et al. (2014) have therefore created a much deeper catalogue ( $cz_{\text{med}} \approx 60\,000 \text{ km s}^{-1}$ ) based on photometric redshifts, (the 2MASS Photometric Redshift catalogue; 2MPZ).

What all these ‘all-sky’ surveys have in common is the lack of information on galaxies hidden behind our own Milky Way due to dust extinction and confusion by high stellar densities. This is what creates the so called zone of avoidance (ZoA; for reviews

\*E-mail: [mpati@astro.rug.nl](mailto:mpati@astro.rug.nl) (MR); [verheyen@astro.rug.nl](mailto:verheyen@astro.rug.nl) (MAW); [kraan@ast.uct.ac.za](mailto:kraan@ast.uct.ac.za) (RCK-K)

see Kraan-Korteweg & Lahav 2000; Kraan-Korteweg 2005). We still have a highly incomplete census of the galaxy distribution in the local Universe along the 360°-circle of the inner ZoA, i.e. for Galactic latitudes  $|b| \leq 5^\circ$ , with a broader ZoA around the Galactic Bulge ( $|b| \lesssim 10^\circ$ ).

Uncovering galaxies in the ZoA is important for studying the kinematics of the Local Group (LG) and large-scale structures (LSSs) in the local Universe. This includes understanding the origin of the dipole observed in the cosmic microwave background (CMB; Fixsen & Kashlinsky 2011). Earlier studies focused on the significance of the Great Attractor (GA) at 45–50 Mpc and the Perseus-Pisces Supercluster (PPS) at 57–114 Mpc as likely contributors (Dressler et al. 1987; Rowan-Robinson et al. 1990; Hudson 1993). More recent studies, however, suggest contributions to the dipole from more distant LSS at  $\sim 200$  Mpc like the Shapley Supercluster (Branchini & Plionis 1996; Plionis & Kolokotronis 1998; Kocevski & Ebeling 2006; Lavaux et al. 2010; Lavaux & Hudson 2011). It has been proposed that incomplete mapping of the ZoA is to a certain degree responsible for these uncertainties (Erdođdu et al. 2006; Loeb & Narayan 2008).

Observing the 21 cm line emission of neutral hydrogen (H I) in gas-rich galaxies is an effective method of mapping the most obscured regions behind the Galactic plane (GP). This is due to the transparency of foreground interstellar dust at this wavelength and the Doppler shift of the emission line. To take advantage of this, considerable efforts have been devoted to H I surveys to find galaxies in the ZoA and measure their redshifts.

Earlier H I surveys of the ZoA include the 91-m Green Bank radio telescope blind survey out to  $\sim 7200$  km s<sup>-1</sup> (Kerr & Henning 1987) and the more systematic Dwingeloo Obscured Galaxy Survey (DOGS; Kraan-Korteweg et al. 1994), with an rms of 40 mJy at a channel width of 4 km s<sup>-1</sup> out to 4000 km s<sup>-1</sup>. The Parkes Multi-beam Receiver has been used to systematically map the ZoA in the Southern hemisphere (HIZOA-S; Staveley-Smith et al. 2016) with an extension to the North (HIZOA-N; Donley et al. 2005) for the most obscured part of the ZoA ( $|b| < 5^\circ$ ). With an rms of  $\sim 6$  mJy and channel width of 13.2 km s<sup>-1</sup> out to  $\sim 12\,000$  km s<sup>-1</sup> these surveys together cover the ZoA from  $\ell = 196^\circ$  across the Galactic Bulge to  $\ell = 52^\circ$ . Another recent and more sensitive survey is the Arecibo L-Band Feed Array Zone of Avoidance Survey (ALFA ZoA; Henning et al. 2010; McIntyre et al. 2015) with an rms of 1 mJy at 9 km s<sup>-1</sup> resolution which is mapping the ZoA accessible to the Arecibo telescope ( $30^\circ \lesssim \ell \lesssim 75^\circ$  and  $175^\circ \lesssim \ell \lesssim 207^\circ$ ). All of these surveys have contributed to uncovering gas-rich galaxies and structures they belong to in the ZoA. However, they have so far left a major part of the Northern ZoA mostly unexplored ( $80^\circ \lesssim \ell \lesssim 180^\circ$ ).

For this reason a systematic H I follow-up pointed survey of 2MASX bright galaxy candidates in the ZoA without previous redshift information ( $\sim 1200$  observed to date) was started with the 100m-class Nançay Radio Telescope (NRT)<sup>1</sup> to an rms of  $\sim 3$  mJy with a velocity resolution of 18 km s<sup>-1</sup> out to  $v \leq 12\,000$  km s<sup>-1</sup> (van Driel et al. 2009; Ramatsoku et al. 2014, Kraan-Korteweg et al., in preparation).

Among features uncovered by the 250 NRT detections was a filament crossing the GP at  $\ell \approx 160^\circ$  with a recession velocity range of 4000–7000 km s<sup>-1</sup> (see fig. 1 in Ramatsoku et al. 2014). Its position and velocity suggest it to be part of the ZoA crossing of the PPS, which had been hypothesized to exist previously (Focardi,

Marano & Vettolani 1984). This structure was earlier mapped with H I-observations of optically identified galaxies (e.g. Chamarax et al. 1990) and tentative indicators for this filament were found, but it was sparsely sampled. This filament encompasses an X-ray galaxy cluster, 3C 129 at  $\ell, b \approx 160:52, 0:28$  (Ebeling et al. 1998; Leahy & Yin 2000). The X-ray cluster hosts two bright radio galaxies, a head-tail source (3C 129) and a double-lobed giant elliptical radio galaxy (3C 129.1), at  $cz = 6236$  and  $6655$  km s<sup>-1</sup>, respectively (Spinrad 1975). The presence of such radio sources usually implies a rich cluster environment. The cluster has a total X-ray luminosity of  $L_X = 1.89 \times 10^{44}$  h<sub>50</sub><sup>-2</sup> erg s<sup>-1</sup> as listed in the ‘Clusters In the ZoA’ survey (CIZA; Ebeling et al. 1998) from the *ROentgen SATellite* (*ROSAT*;<sup>2</sup> Truemper 1982). While not the most luminous *ROSAT* X-ray cluster listed, it should be noted that it might be more massive than suggested by its X-ray luminosity since the intervening high Galactic gas column density ( $N_{\text{H}} \approx 5.76 \times 10^{21}$  cm<sup>-2</sup>; Stark et al. 1992) may well have reduced the X-ray flux in the *ROSAT* 0.2–2.4 keV band by more than 30 per cent (Leahy & Yin 2000).

Due to the high extinction layer of the Milky Way, most of the galaxies belonging to this cluster had not been observed before. Hence we decided to conduct a deep blind H I imaging survey with the Westerbork Synthesis Radio Telescope<sup>3</sup> (WSRT) of a mosaic covering a 9.6 deg<sup>2</sup> sky area which comprises the cluster and the surrounding filament within which the NRT survey showed it to be embedded.

Our aims are to first investigate in detail the structure associated with the 3C 129 galaxy cluster. The H I data and accompanying near-infrared photometry will give distance estimates using the Tully–Fisher relation. These will be used to determine the cluster’s relevance to flow fields around it and the larger Perseus-Pisces Complex, notably evident in the whole-sky 2MASS depictions of the LSS that appears to pierce the cluster as it crosses from the Southern to Northern Galactic hemispheres (Jarrett 2004). Moreover, these data will aid the 2MASS Tully–Fisher survey (2MTF; Masters, Springob & Huchra 2008) efforts, by complementing the inner  $b \approx |5^\circ|$  ZoA regions excluded from optical spectroscopy. Secondly, taking advantage of the wide areal coverage of our H I imaging survey of the cluster and its environments, we will be able to conduct an examination of environmental effects on the H I properties of these galaxies.

A further aspect of this project is to provide interferometric data cubes to assess data handling algorithms such as pipeline reduction, calibration, source finding and characterization. Having a good handle on these algorithms will prove invaluable in the planning and preparation of the forthcoming H I surveys to be carried out with AperTIF at the WSRT (Verheijen et al. 2008; Oosterloo, Verheijen & van Cappellen 2010) and SKA precursor instrument H I surveys to be conducted with MeerKAT and ASKAP (de Blok 2011; Duffy et al. 2012, respectively). It is for this reason that our velocity search range (2400–16 000 km s<sup>-1</sup>), extends far beyond the mean velocity of the 3C 129 cluster.

In this first of a series of papers based on the WSRT imaging survey described above, we present the H I data of the galaxies unveiled in the ZoA, both as a catalogue containing H I parameters as well as an atlas of H I distributions and kinematics. We also include a discussion of the LSSs traced by the detected galaxies. Subsequent papers will focus in detail on the other aforementioned science goals.

<sup>2</sup> <http://www.xray.mpe.mpg.de/cgi-bin/rosat/rosat-survey>

<sup>3</sup> <http://www.astron.nl/radio-observatory/>

<sup>1</sup> <http://www.nrt.obspm.fr/>

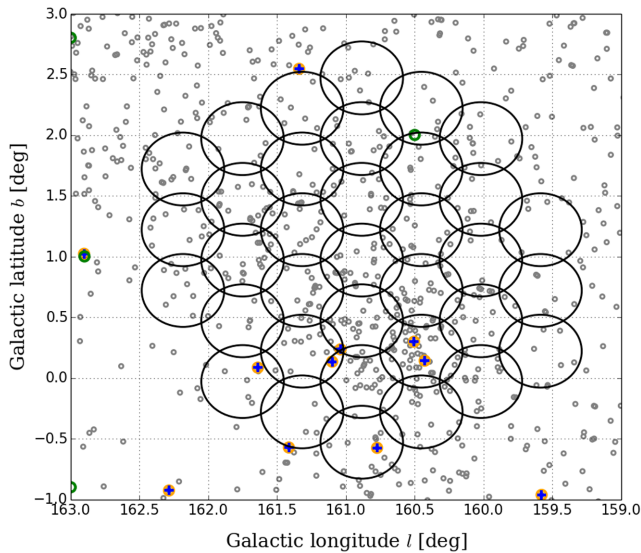


**Figure 1.** The projected sky distribution of the observed hexagonal mosaic. The circles indicate the HPBW of the individual WSRT pointings. The small grey circles show the 2MASX near-infrared extended sources within this region, highlighting the 3C 129 cluster centred at  $l, b \approx 160^{\circ}52, 0^{\circ}28$ . The orange open circles and blue crosses mark seven galaxies within the observed area with redshifts listed in NED and HyperLEDA, respectively. Galaxies with H<sub>1</sub> detections from the NRT survey are shown in green open circles.

This paper is organized as follows: in Section 2 we describe the observing strategy and WSRT data reduction. Section 3 provides a description of our source finding procedure. Methods used to determine the H<sub>1</sub> properties of detected galaxies are described in Section 4. The resulting H<sub>1</sub> atlas products are described in Section 5, while the full atlas is presented as supplementary material available online. Also in Section 5, the completeness of the survey and counterparts search are discussed. In Section 6 we discuss the measured H<sub>1</sub> parameters and their characteristics. Lastly, structures revealed by this survey are presented in Section 7.

We assume a  $\Lambda$  cold dark matter cosmology with  $\Omega_M = 0.3$ ,  $\Omega_\Omega = 0.7$  and a Hubble constant  $H_0 = 70 \text{ km s}^{-1} \text{ Mpc}^{-1}$  throughout this paper.

## 2 OBSERVATIONS AND DATA REDUCTION

Observations were carried out using the WSRT between 2012 August and November. We imaged a mosaic comprising 35 fields arranged in a hexagonal grid covering  $9.6 \text{ deg}^2$ , each separated by  $\Delta = 0.5$ . This setup is similar to that of a single AperTIF phased array feed pointing, minus two fields. In Fig. 1, we present the layout of the mosaic with positions of galaxies from the literature shown in this field. We chose this particular mosaic grid to be able to cover the largest possible field of view with an acceptable noise variation of 20 per cent between pointing centres. The total sky area covered is large enough to map the network between the PPS filament and the 3C 129 cluster.

Each field was observed for a total on-source integration time of  $2 \times 6 \text{ h}$ , in between half-hour long pre- and post-calibrations. We obtained data in eight IF-bands per pointing, each 10 MHz wide, with 256 channels in dual polarization mode, overlapping by 16 per cent in frequency. This configuration covered a total effective bandwidth of 67 MHz with 1717 channels that are 39 kHz ( $8.25 \text{ km s}^{-1}$ ) wide at  $z = 0$ . We therefore cover a velocity range

of  $cz = 2400\text{--}16\,600 \text{ km s}^{-1}$  corresponding to a volume depth of about 214 Mpc. Therefore we map our main target with acceptable velocity resolution while still being able to survey the more distant Universe. The total volume surveyed is  $26\,300 \text{ Mpc}^3$ .

The survey configuration allows the detection of galaxies with H<sub>1</sub> masses greater than  $M_{H_1} = 3.0 \times 10^8 M_\odot$  at the median distance of the PPS ( $cz \approx 6000 \text{ km s}^{-1}$ ), assuming a line width of  $150 \text{ km s}^{-1}$  at the  $6\sigma$  noise level such that we could attain acceptable statistics to map the cluster.

The observational parameters for the 35 pointings are summarized in Table 1. Column 1 gives the pointing number. Columns 2 and 3 and columns 4 and 5 are the central equatorial and Galactic coordinates of the pointings, respectively. The synthesized beam sizes and position angles are given in columns 6 and 7, respectively. In column 8, the average rms noise for each pointing is given. Column 9 gives the flux densities of the brightest continuum sources in each pointing.

### 2.1 Data processing

The UV-data were flagged, calibrated and Fourier transformed using the NRAO Astronomical Imaging Processing System package<sup>4</sup> (AIPS; Greisen 1990; van Moorsel, Kemball & Greisen 1996).

#### 2.1.1 RFI flagging, amplitude and phase calibration

Telescope-based gain and phase corrections were determined by observing the standard calibrators 3C 48 (J0137+331) with a flux density of 15.56 Jy and 3C 147 (J0542+498) with a flux density of 21.58 Jy. After loading the UV-data into AIPS, the system temperature ( $T_{\text{sys}}$ ) was checked to assess the behaviour of antennas throughout the observation, followed by applying the time-dependent  $T_{\text{sys}}$  corrections. In all cases solar interference was excised from the observations by deleting visibilities from the short 9A, 9B and AB baselines for time ranges during which the Sun was above the horizon. This measure is justified by the expected small sizes of our target sources. Additionally, Radio Frequency Interference (RFI) that affected flux and phase calibrators were flagged using the *clip* task which flags RFI by searching for amplitudes that are out of range. For the calibrators 3C 48 and 3C 147 we clipped amplitudes that were above 23 Jy and 29 Jy, respectively, after which we conducted an automated frequency dependent RFI flagging using *rflag*. In total, about 5 per cent of all the UV-data was flagged. Gain and phase solutions were then determined and transferred to the visibility data of the science targets. The same calibrators were used for bandpass corrections. First, rough bandpass (BP) solutions were determined (task *bpass*) and examined. This was followed by further RFI flagging, if any, and the production of new BP solutions. The process was repeated, each time improving on the BP solutions. Once satisfied with the calibration results, we applied these to the UV-data of the science target. No self-calibration was performed.

#### 2.1.2 Imaging data cubes

The calibrated UV-data sets were Fourier transformed into image cubes using the *imgr* task. For each pointing, eight data cubes were made as per the number of IF bands. The size of each image was  $512 \times 512$  pixels with a pixel size of  $6 \text{ arcsec} \times 6 \text{ arcsec}$  and

<sup>4</sup> <http://www.aips.nrao.edu/index.shtml>



**Table 1.** Observing parameters of the WSRT PP ZoA survey.

Field	R.A (J2000)	Dec (J2000)	$\ell$	$b$	Synth. beam	PA	rms noise	Cont. sources
(1)	hh:mm:ss.ss	dd:dm:ds.ss	°	°	arcsec $\times$ arcsec	°	mJy beam <sup>-1</sup>	mJy
(1)	(2)	(3)	(4)	(5)	(6)	(7)	(8)	(9)
01 <sup>a</sup>	04:49:34.85	45:02:32.89	160.452	0.220	21.2 $\times$ 15.2	2.0	0.37	4001, 935
02 <sup>b</sup>	04:47:25.35	44:43:13.83	160.452	-0.280	22.9 $\times$ 16.1	1.3	0.41	4001, 935
03 <sup>c</sup>	04:46:54.93	45:12:44.14	160.019	-0.030	21.8 $\times$ 16.3	4.1	0.35	4001, 935
04	04:49:05.37	45:32:05.54	160.019	0.470	23.2 $\times$ 16.4	1.6	0.38	4001, 935, 703
05	04:51:45.83	45:21:42.96	160.452	0.720	23.4 $\times$ 16.4	4.7	0.41	4001, 935
06	04:52:13.84	44:52:07.62	160.885	0.470	23.8 $\times$ 16.3	0.0	0.36	4001, 935
07	04:50:03.82	44:32:59.77	160.885	-0.030	23.3 $\times$ 16.3	1.1	0.41	4001, 935, 414
08	04:54:25.33	45:11:06.33	160.885	0.970	23.4 $\times$ 16.6	1.1	0.38	
09	04:53:58.31	45:40:43.68	160.452	1.220	23.2 $\times$ 16.6	1.2	0.38	
10	04:54:51.88	44:41:28.59	161.318	0.720	24.3 $\times$ 16.7	1.7	0.39	426
11	04:57:03.82	45:00:15.90	161.318	1.220	24.3 $\times$ 16.7	1.6	0.40	703, 414
12	04:56:38.28	45:29:55.52	160.885	1.470	23.4 $\times$ 16.3	-0.1	0.38	426
13	04:59:17.21	45:18:53.53	161.318	1.720	23.5 $\times$ 16.3	0.1	0.38	426
14	04:52:41.37	44:22:31.99	161.318	0.220	22.8 $\times$ 17.3	12.6	0.38	414
15 <sup>d</sup>	04:51:17.33	45:51:17.74	160.019	0.970	22.4 $\times$ 17.3	14.2	0.40	703
16	04:58:52.69	45:48:34.80	160.885	1.970	23.3 $\times$ 16.7	1.0	0.41	703
17	04:59:41.29	44:49:11.95	161.751	1.470	23.7 $\times$ 16.7	1.7	0.38	426
18	04:57:28.93	44:30:36.07	161.751	0.970	23.9 $\times$ 16.6	2.0	0.38	343
19	04:56:12.28	45:59:34.63	160.452	1.720	23.2 $\times$ 16.7	1.6	0.39	414
20	04:55:17.98	44:11:50.75	161.751	0.470	24.3 $\times$ 16.6	1.1	0.40	703
21	04:50:32.30	44:03:26.40	161.318	-0.280	24.1 $\times$ 16.6	2.1	0.40	426, 343
22 <sup>e</sup>	04:48:35.38	46:01:37.44	159.586	0.720	21.7 $\times$ 17.0	5.5	0.45	
23	04:53:30.82	46:10:20.35	160.019	1.470	21.5 $\times$ 16.3	4.3	0.42	
24	04:47:55.26	44:13:43.16	160.885	-0.530	24.3 $\times$ 16.6	1.3	0.37	426
25	04:46:23.99	45:42:13.80	159.586	0.220	23.5 $\times$ 16.6	1.2	0.37	703, 414
26	04:58:27.75	46:18:15.45	160.452	2.220	23.6 $\times$ 17.1	3.6	0.40	426
27	05:01:32.02	45:37:21.12	161.318	2.220	23.9 $\times$ 17.0	3.1	0.39	426
28	05:01:55.06	45:07:38.02	161.751	1.970	23.7 $\times$ 16.7	1.9	0.38	414
29	05:00:04.97	44:19:30.33	162.184	1.220	24.0 $\times$ 16.6	1.7	0.37	703
30	04:57:53.61	44:00:56.31	162.184	0.720	24.2 $\times$ 16.6	0.9	0.40	703
31	04:53:08.43	43:52:56.36	161.751	-0.030	24.2 $\times$ 16.6	1.0	0.40	426
32	04:50:48.33	46:20:51.66	159.586	1.220	23.1 $\times$ 16.7	1.2	0.39	343
33	04:55:45.82	46:29:12.97	160.019	1.970	23.0 $\times$ 16.7	0.7	0.38	414
34	05:01:08.57	46:07:03.79	160.885	2.470	23.3 $\times$ 16.7	1.2	0.38	703
35	05:02:17.70	44:37:54.77	162.184	1.720	24.3 $\times$ 16.8	0.8	0.37	426, 343

<sup>a</sup>3C 129 and 3C 129.1 (centred)<sup>b,c</sup>3C 129 and 3C 129.1 (off-centred)<sup>d,e</sup>RFI on all short baselines

256 channels. They were made using a *robust* weighting scheme set to 0.4, this being the best trade-off between the WSRT beam size and rms noise. Dirty beam image cubes corresponding to the antenna patterns were made for CLEANING purposes. They were 1024  $\times$  1024 pixels in size, twice that of the image cubes. Since this is a blind survey, with the location of the H I emission not known beforehand, no CLEANING and continuum subtraction were done before or during the imaging process.

### 2.1.3 Continuum subtraction

The removal of continuum sources as well as their instrumental responses from the data cubes was performed in the image plane for each of the eight IF bands in each cube using the Groningen Image Processing SYstem (GIPSY; van der Hulst et al. 1992). As an initial step the strongest continuum sources were masked and CLEANED. The initial CLEANING was conducted to mitigate the variability of their sidelobes from channel to channel, caused by the frequency dependent RFI flagging. This was followed by fitting a zeroth-order polynomial baseline to the spectrum at each pixel including possible H I emission. After this initial baseline fit and subtraction,

the rms noise per channel of each continuum-subtracted channel map was inspected. Data points above and below a chosen rms noise level were clipped and excluded from successive baseline fits. This procedure was repeated, each time increasing the baseline fit order until the third order was reached, whilst gradually decreasing the rms noise clip levels down to  $\pm 2\sigma$  so as to exclude the faint H I emission from the baseline fitting. The final 35 image cubes were produced by combining the eight IF bands for each pointing, excluding the first 5 and last 36 channels in each cube due to increased noise levels after the bandpass correction.

Fig. 2 shows the rms noise as a function of velocity after continuum subtraction and Hanning smoothing in velocity. We achieved an average rms noise of 0.36 mJy beam<sup>-1</sup> per channel, for a resolution of 16.5 km s<sup>-1</sup>, with a frequency dependent variation of less than 20 per cent on average over the observed velocity range. This variation is due to RFI residuals as well as the bandpass roll-off at the edge of the IF bands and the 17 MHz standing wave ripple. Additionally, 2 of the 35 pointings had severe residual RFI on all short baselines (i.e. less than 144 m) which resulted in those baselines being completely flagged, hence increasing the noise in those cubes. Flagging all short baselines in these pointings decreased our

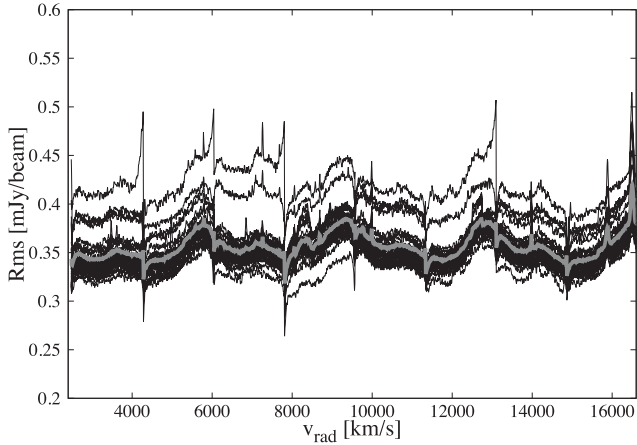


**Figure 2.** The rms noise as a function of velocity in the 35 cubes after continuum subtraction and RFI flagging. The average noise level in each individual cube is mostly uniform at  $0.36 \text{ mJy beam}^{-1}$  over the whole observed velocity range. The average rms noise of all the individual cubes is illustrated by the thick grey line. Variations in the rms noise are frequency-dependent and caused by the bandpass roll-off in the overlapping regions of the eight IF bands, RFI residuals and the 17 MHz standing wave ripple. The increased rms noise in two of the fields is caused by severe RFI, which resulted in complete flagging of all their short baselines.

inner UV coverage, which reduced the size of the largest structures to which our observations are sensitive. For instance in these fields we are sensitive to structures up to 7 arcmin in size, which is about  $4\times$  smaller than what we would be sensitive to without RFI on the short baselines.

#### 2.1.4 CLEANING and mosaicking

To remove sidelobes of the synthesized beam, each of the 35 cubes were first CLEANED blindly to the  $5\sigma$  noise level to remove the sidelobes from the brightest sources. The clean components were then restored with a Gaussian beam of  $23 \text{ arcsec} \times 16 \text{ arcsec}$  FWHM (PA =  $0^\circ$ ). We then conducted a source finding procedure, as described in Section 3. The procedure resulted in defining those areas within the cube that contain only the identified H<sub>1</sub> signal in each channel. These areas were then used as masks to perform a new CLEAN image deconvolution down to the  $0.33\sigma$  noise level. The final CLEANED cubes were combined into a mosaic to improve the sensitivity of the survey within the overlapping regions of the pointings. Mosaicking was conducted using the *flatn* task in AIPS which combines image cubes produced by *imgr*. Overlapping regions of images were averaged with a weighting scheme that accounts for the primary beam attenuation and the number of flagged visibilities.

An example of typical spatial noise variations in a mosaicked channel map, measured for each pixel over a range of 50 channels (nos 411–460, i.e. the velocity range of 6903–7307  $\text{km s}^{-1}$ ) in the full primary-beam corrected mosaic is shown in Fig. 3. In these channels the average rms noise is  $\sim 0.4 \text{ mJy beam}^{-1}$  in the central region (black box in Fig. 3). It increases to  $0.8 \text{ mJy beam}^{-1}$  towards the edges due to the applied correction for primary-beam attenuation. Fig. 4 shows histograms of the spatial noise distribution for the primary-beam corrected mosaic (light grey) and the uncorrected mosaic (dark grey) in these channels as measured inside the area outlined by the black box. As expected, after applying the primary-beam correction, the peak of the distribution shifts to higher noise values while the distribution becomes broader.

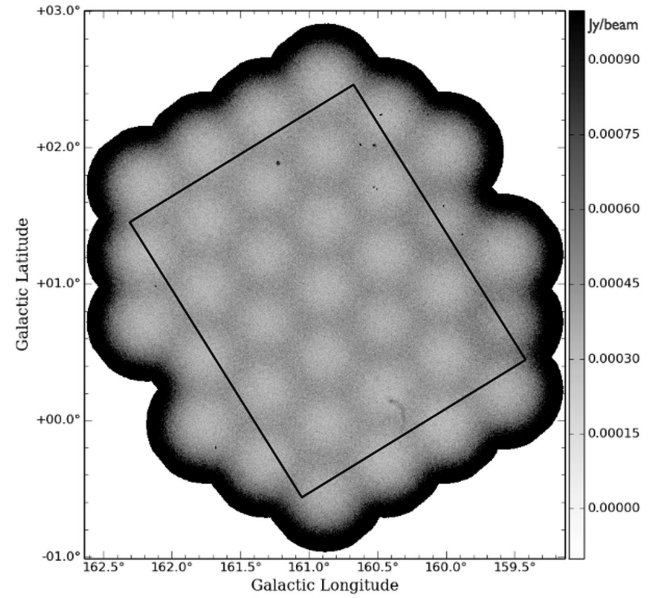


**Figure 3.** An illustration of the spatial noise variation over 50 channels (nos 411–460, or 6903–7307  $\text{km s}^{-1}$  in radial velocity) out of the 1717 channels in our full, primary-beam corrected WSRT survey mosaic. Note the increase in the noise near the edges due to the applied correction for primary-beam attenuation. The black box outlines the inner region within which the spatial noise distributions, shown in Fig. 4, were calculated. The rms noise level values in  $\text{Jy beam}^{-1}$  are shown by the grey-scale bar.

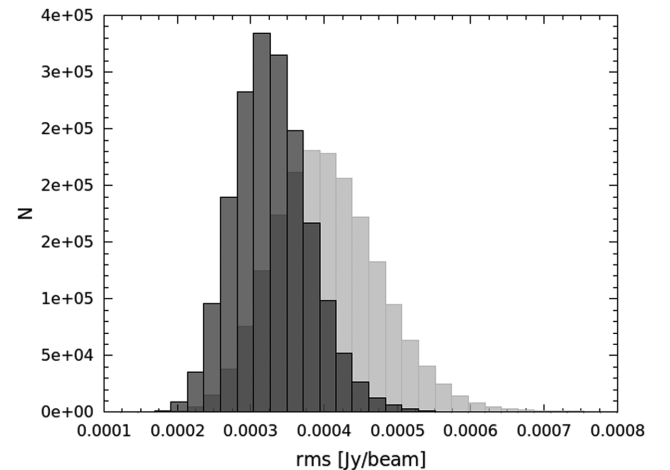


**Figure 4.** An illustration of the effect of the primary beam correction on the rms noise distribution. Histograms of the rms noise distribution measured over 50 channels within the inner regions (outlined by the black box in Fig. 3) of our full WSRT survey mosaic. The light grey distribution is measured from the primary-beam corrected mosaic and the dark grey from a mosaic without the primary-beam corrections.

### 3 SOURCE FINDING

Before compiling the list of sources detected, we investigated characteristics of the pixel value distribution in each of the 35 individual cubes without primary beam corrections so as to avoid spatial noise variations in the mosaicked cube, as illustrated by the light grey histogram in Fig. 4. We found four distinct trends in the distributions as illustrated in Fig. 5. The top panel displays the behaviour of the noise when there are neither imaging artefacts nor H<sub>1</sub> detections. Pixel values are then symmetrically distributed and near Gaussian.

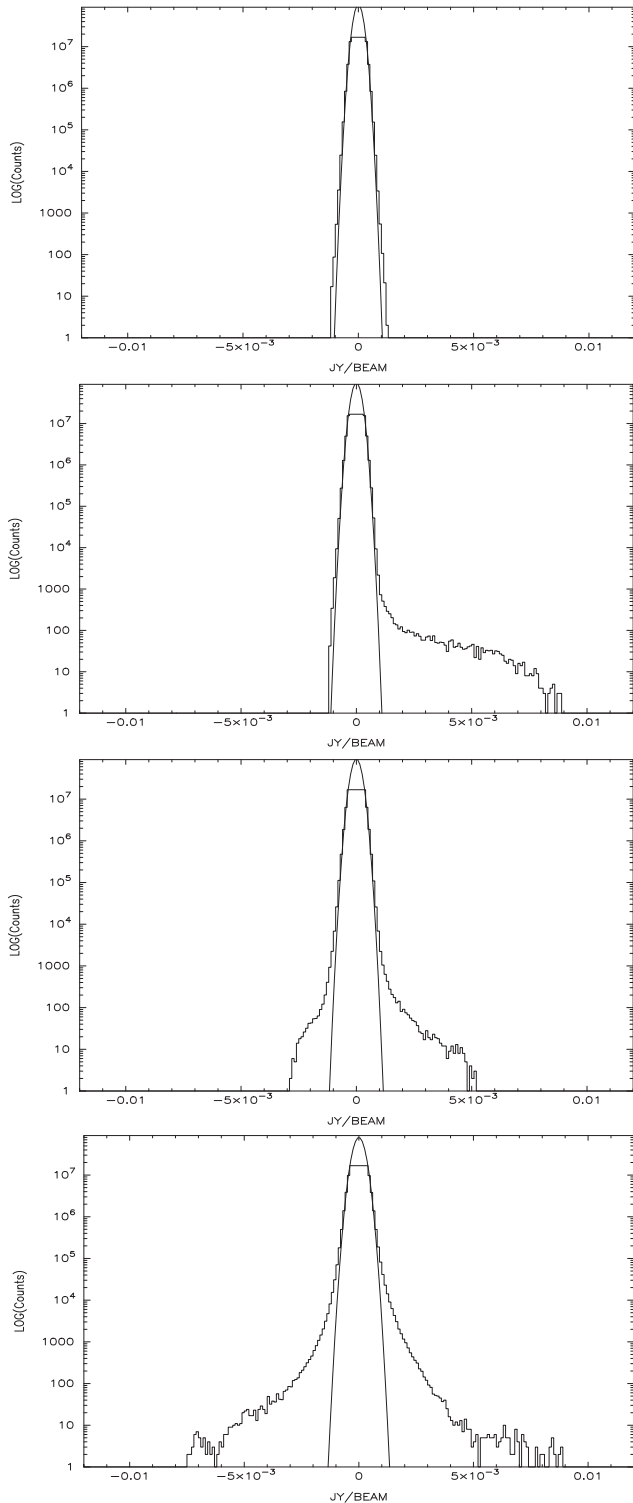


**Figure 5.** Statistics of pixel values in individual cubes with a Gaussian curve overlaid, illustrating the four distinct characteristic cases identified. The top panel represents cases where there are neither imaging artefacts nor H I detections. In the second panel there are no imaging artefacts but many H I detections. The third panel illustrates cases in which there are imaging artefacts as well as H I detections. The bottom panel represents cases where there are no H I detections but many imaging artefacts and RFI residuals.

However, in cases where there are no imaging artefacts, but many H I detections (second panel), the pixel distribution is heavily skewed to positive pixels. Most sources detected in cubes with these characteristics are expected to be real. The third panel shows a negative and a more extended positive wing, representing cases where there are artefacts in the cube as well as real sources. The bottom panel shows a case with RFI residuals and imaging artefacts but no H I detections. In the latter two cases the wings are near symmetric and the positive peaks are unlikely to be due to real sources. Examples of representative imaging artefacts in the data cubes are shown in Fig. 6. The left-hand panel shows gain calibration errors over only about 10 channels during half of the observation. The middle panel shows the effect of an imperfect bandpass after continuum subtraction. The right-hand panel shows horizontal stripes due to remaining RFI. There was no one dominant source that caused these artefacts.

To find H I line emission from galaxies in the mosaicked cube, the spatial variation of the noise was largely removed by multiplying it by the weights cube given by  $(1/\sigma^2)$ , where  $\sigma$  is the weighted noise in each pointing. Source finding was then conducted in several steps using the GIPSY software. First, the high resolution cube ( $23 \text{ arcsec} \times 16 \text{ arcsec}$ ) was smoothed to a beam size of  $30 \text{ arcsec} \times 30 \text{ arcsec}$  (bs30). Secondly, the high resolution and bs30 cubes were smoothed in velocity to four different resolutions, starting with Hanning smoothing (R2;  $16.5 \text{ km s}^{-1}$ ) followed by a Gaussian smoothing kernel such that the FWHM of the resulting near-Gaussian spectral response function corresponds to four (R4;  $33 \text{ km s}^{-1}$ ), six (R6;  $49.5 \text{ km s}^{-1}$ ) and eight (R8;  $66 \text{ km s}^{-1}$ ) channels, respectively. No downsampling in spatial pixels or velocity channels was done after smoothing. Each of the 35 cubes was then searched at all eight different angular/velocity resolution combinations. Thirdly, for each resolution combination, channel maps were clipped at 8, 5, 4 and 3 times the rms noise level per channel. Lastly, a detection was accepted if it occurred at  $8\sigma$  in a single velocity resolution element (i.e. in  $n$ -channels for  $R_n$ ), at  $5\sigma$  in two adjacent velocity resolution elements ( $2 \times n$  channels for  $R_n$ ), at  $4\sigma$  in three adjacent velocity resolution elements and at  $3\sigma$  in four adjacent velocity resolution elements. All channels within a velocity resolution element had to be above the specified noise clip level. All the pixels containing the H I signal were combined into three-dimensional masks. This automated source finding method resulted in 683 potential galaxy detection candidates.

A follow-up visual examination of all potential H I detections was conducted independently by two persons. This resulted in the rejection of a total of 235 as imaging artefacts due to residual RFI and side lobes of continuum sources (see Fig. 6 for examples). These artefacts occurred predominantly in the two pointings which had all short baselines removed due to RFI. As a result 90 per cent of the automatically detected sources in these two pointings were rejected. This is not too severe because the two pointings with short baselines removed represent only a negligible fraction (0.1 per cent) of all visibilities and (0.03 per cent) of our total survey volume, while the affected data are still sensitive to structures up to  $\sim 7$  arcmin in size. The resulting list contained 448 remaining candidates. Visual inspection steps were taken to differentiate between real sources and those that resemble noise peaks in this list. We further removed 237 sources which were consistent with noise peaks or imaging artefacts based predominantly on their signal to local noise ratio. This led to a final detection list of 211 galaxies.



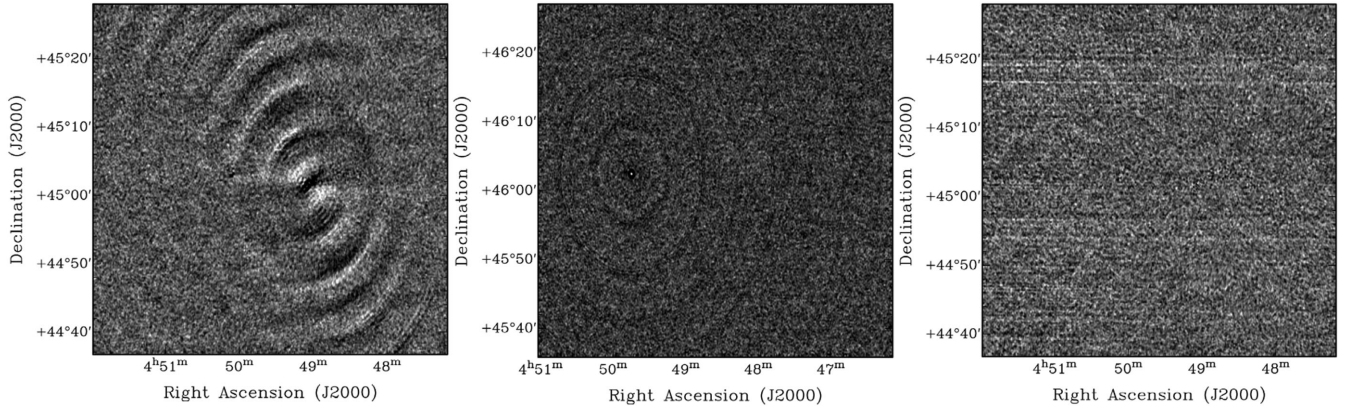


**Figure 6.** Examples of various types of imaging artefacts in the data cubes. The left-hand panel shows artefacts caused by gain calibration errors over a small number of channels during half of the observation of the respective pointing. The middle panel shows artefacts due to bandpass imperfections after continuum subtraction. The right-hand panel shows stripes caused by remaining RFI.

## 4 DATA PRODUCTS OF DETECTED H I SOURCES

In this section we describe the methods used to determine the H I properties of galaxies detected. The structure of the H I catalogue and the atlas of the detections is discussed in Section 5.

### 4.1 The global H I profiles

The global H I profiles were made from the primary-beam corrected flux within the channel-dependent H I emission masks of the detected galaxies at the  $16.5 \text{ km s}^{-1}$  velocity resolution. Each profile was then partitioned into three velocity bins of equal width, referred to as the receding (*r*), the middle (*m*) and approaching (*a*) bins. We then determined the peak flux densities ( $F^p$ ) in the three velocity bins as  $F_r^p$ ,  $F_m^p$  and  $F_a^p$ , respectively. The three values were used to categorise the shape of the global profile as double-horned if  $F_r^p > F_m^p < F_a^p$ , Gaussian if  $F_r^p < F_m^p > F_a^p$  and otherwise as asymmetric. For the double-horned profiles the peak flux densities on both the receding (*r*) and approaching (*a*) sides were considered separately for calculating their 20 per cent and 50 per cent levels. In the Gaussian and asymmetric cases only the absolute peak flux density was used. We then linearly interpolated between the data points from the profile centre outward to determine the velocities ( $v_{r,20}$ ,  $v_{a,20}$ ,  $v_{r,50}$ ,  $v_{a,50}$ ) corresponding to levels at 20 per cent and 50 per cent of the peak flux densities. It should be noted however, that for H I profiles with edges that are not consistently decreasing, this method tends to slightly underestimate the line widths.

The systemic velocity is determined according to

$$v_{\text{sys}} = 0.25(v_{r,20} + v_{a,20} + v_{r,50} + v_{a,50}) \quad (1)$$

The profile line widths are measured using

$$w_{20} = v_{r,20} - v_{a,20} \quad (2)$$

$$w_{50} = v_{r,50} - v_{a,50} \quad (3)$$

The total H I flux ( $S_{\text{int}}$ ) in  $\text{Jy km s}^{-1}$  was determined by integrating the global profiles according to;

$$S_{\text{int}} = \sum S_v \Delta v \quad (4)$$

where  $S_v$  is the H I flux density in Jy at each channel and  $\Delta v$  is the channel width in  $\text{km s}^{-1}$ .

For a particular galaxy, especially if it is spatially resolved, the size, shape and position of the H I clean mask changes from channel

to channel due to the rotating H I disc. Thus the uncertainty in the flux also varies from channel to channel. To calculate the uncertainty in the flux of a global H I profile at each channel, we replicated the clean mask that encloses the H I emission and projected this at eight different line-free positions surrounding the detection. We then measured the signal in each of the eight projected masks and defined the uncertainty in the line flux from the galaxy as the rms scatter in the eight flux measurements in the projected masks.

### 4.2 Total H I maps

The total H I maps, showing the H I column density distributions were made using the CLEAN masks that define the H I emission from the CLEANED data cubes. These data cubes were corrected for primary beam attenuation. Pixels outside the CLEANED mask were set to zero and pixels inside the masks were summed up to build the H I maps. The advantage of this method is an attained higher signal-to-noise ratio at some pixels of the H I map. It does however, result in a non-uniform noise distribution across the map such that the  $3\sigma$  column density level cannot be defined. We converted the pixel value of the H I map to column densities (in  $\text{atoms cm}^{-2}$ ) using

$$N_{\text{H I}} = 1.82 \times 10^{18} \int T_b dv \quad (5)$$

where  $T_b$  is the brightness temperature in Kelvin and  $dv$  is the channel width in  $\text{km s}^{-1}$  of the integrated H I emission line. For our survey, a typical  $N_{\text{H I}}$  sensitivity at the  $3\sigma$  level is  $5.3 \times 10^{19} \text{ cm}^{-2}$  where  $dv = 16.5 \text{ km s}^{-1}$ .

The total H I mass of a galaxy (in  $M_{\odot}$ ) was determined by calculating:

$$M_{\text{H I}} = 2.36 \times 10^5 D^2 \int S_v dv \quad (6)$$

where  $D$  is the distance to the galaxy in Mpc measured according to

$$D = \frac{v_{\text{sys}}}{H_0} \quad (7)$$

where  $H_0$  is the Hubble constant and  $\int S_v dv$  is the integrated global H I profile flux in  $\text{Jy km s}^{-1}$ .

We fitted a two-dimensional Gaussian function to the H I map of each of the 211 detections. We then estimated the H I size ( $D_{\text{H I}}$ ) as defined by the fitted Gaussian's major ( $\Theta_{x,g}$ ) and minor ( $\Theta_{y,g}$ ) axis FWHM in arcseconds such that  $D_{\text{H I}} = \sqrt{\Theta_{x,g} \times \Theta_{y,g}}$ . The



H I size ( $D_{\text{H I}}$ ) was then compared to that of the WSRT beam,  $D_{\text{WSRT}} = \sqrt{\Theta_x \times \Theta_y}$ , where  $\Theta_x$  and  $\Theta_y$  are the beam FWHMs of 23 arcsec and 16 arcsec, respectively. An H I detection was defined as spatially resolved if  $D_{\text{H I}}$  exceeded  $1.5 \times D_{\text{WSRT}}$ , otherwise it is considered marginally resolved. The resulting position angles of the fitted Gaussians were not corrected for the minimal effect of the slightly elongated synthesized beam which is oriented exactly North–South. The distribution of fitted position angles, however, does not show an excess of North–South orientations.

### 4.3 Radial column density profiles

For the spatially resolved galaxies, the radial H I column density profiles were extracted from the total H I maps in which the pixel column density units were converted to  $M_{\odot} \text{pc}^{-2}$ , by azimuthally averaging non-blank pixels in concentric elliptical annuli with radii along the semi-major axis of 5, 15, 25, 35, . . . , 105 arcsec with a width of 10 arcsec and centred on the H I-centroid position of the galaxy. This position was defined as the centroid of the two-dimensional Gaussian function fitted to the total H I map as described in Section 4.2. No corrections for beam smearing were applied. We averaged over the receding and approaching side separately to identify possible asymmetries. From the radial profiles, the H I radius ( $R_{\text{H I}}$ ) in kpc was measured as the radius where the mean surface density ( $\Sigma_{\text{H I}}$ ) drops to  $1 M_{\odot} \text{pc}^{-2}$ .

### 4.4 H I velocity fields

The velocity fields of the spatially resolved H I discs were produced by fitting a Gaussian to the R2.bs30 velocity profile at each pixel. The fitting algorithm used initial estimates for the amplitude, central velocity and velocity dispersion of the Gaussian function. The initial amplitude estimate simply is the peak flux density, whereas the initial estimates for the velocity centroid and dispersion are based on the flux-weighted first and second moment of the non-blank pixel profile, respectively. The advantage of fitting Gaussians instead of measuring the standard flux-weighted moments is that we can specify ranges within which the fitted parameters and their uncertainties must lie in order for a fit to be accepted. Fits were accepted only if (1) the central velocity lies within the H I mask, (2) the uncertainty in the velocity centroid is less than  $10 \text{ km s}^{-1}$ , and (3) the velocity dispersion lies within the range of  $5\text{--}50 \text{ km s}^{-1}$ . This approach, however, does result in velocity fields that are patchy with holes where the signal-to-noise ratio is too low to obtain an acceptable fit.

### 4.5 Position–velocity diagrams

A position–velocity diagram (PVD) illustrates the shape of a projected rotation curve and the presence of a possible kinematic asymmetry of the rotating gas disc. Ideally, a PVD should be extracted along the kinematic major axis of an inclined rotating disc and centred on its dynamical centre. Usually, this geometry is derived from two-dimensional velocity fields which are available only for the spatially resolved galaxies in our survey. Hence we followed different strategies for the resolved and marginally resolved galaxies.

For the PVDs of the resolved galaxies in our survey we estimated by eye the position angle of the receding side of the kinematic major axis by considering the direction perpendicular to the kinematic minor axis indicated by the green isovelocity contour of the velocity field depicted in the accompanying atlas. No detailed analysis of the velocity fields was carried out as this is planned for a

forthcoming publication. The dynamical centres of the rotating gas discs were not derived from their two-dimensional velocity fields but instead were assumed to coincide with the morphological centre of the UKIDSS image (see Section 4.6). In those cases where an infrared counterpart could not be identified, the dynamical centre was assumed to coincide with the centroid of the Gaussian function fitted to the H I column density map.

For the PVDs of the marginally resolved galaxies we adopted the centroid and position angle of the two-dimensional Gaussian fitted to the H I column density maps. In those cases where an infrared counterpart could be identified, we adopted the morphological centre of the UKIDSS image as the dynamical centre of the PVD. In case the UKIDSS image showed a clear elongation, we estimated by eye the position angle of the infrared image and adopted this as the kinematic major axis. For the marginally resolved galaxies, uncertainties in the exact position angle and dynamical centre have little effect on the PVD.

We extracted the PVDs from the Hanning smoothed cubes (R2) as well as from the cubes smoothed to  $66 \text{ km s}^{-1}$  resolution (R8), both at the  $23 \text{ arcsec} \times 16 \text{ arcsec}$  angular resolution

### 4.6 Counterparts

The sky area covered by our survey has a Galactic foreground extinction in the *B*-band of up to  $A_B \sim 4.5 \text{ mag}$ . This makes optically identifying galaxies very difficult. However, the near-infrared wavelength opens a more transparent window since the extinction is less severe. We searched for NIR counterparts in the *K*-band images of the UKIRT Infrared Deep Sky Survey (UKIDSS; Hewett et al. 2006; Lawrence et al. 2007; Casali et al. 2007; Hambly et al. 2008). ‘UKIDSS uses the UKIRT Wide Field Camera (WFCAM; Casali et al. 2007) and a photometric system described in Hewett et al. 2006. The pipeline processing and science archive are described in Irwin et al (2008) and Hambly et al. 2008. We used data from the 10th Galactic Plane Survey (GPS) data release, which is described in detail in Lucas et al. 2008’.<sup>5</sup> The WSRT PP ZoA survey overlaps with the UKIDSS GPS (Lucas et al. 2008) which has mapped  $1800 \text{ deg}^2$  of the Northern GP to a *K*-band depth of  $K = 19.0 \text{ mag}$  (AB system).

The UKIDSS images were searched in two steps. First, the UKIDSS GPS catalogue was searched for galaxy counterpart candidates that were within 1 arcmin radius of the H I positions. Only candidates closest to the H I positions were considered as likely counterparts. These were then verified by a visual inspection of UKIDSS GPS images within the search radius in the *J*, *H* and *K* bands (pixel size of 0.2 arcsec). Secondly, to ensure that no potential counterparts were missed, the search radius was increased to 2 arcmin. For this step, only those H I positions without a verified galaxy counterpart in the first step were cross-checked and verified by visual inspection as well. In some cases a UKIDSS image could not be used due to imaging artefacts. We then searched for 2MASS images instead, in the same manner as for UKIDSS.

Of all H I detected galaxies, 62 per cent were found to have at least one near-infrared counterpart in the UKIDSS GPS catalogue, with an average offset of 2.6 arcsec from the H I position. The other 38 per cent did not show any plausible counterpart close to the H I position.

<sup>5</sup> <http://www.ukidss.org/>

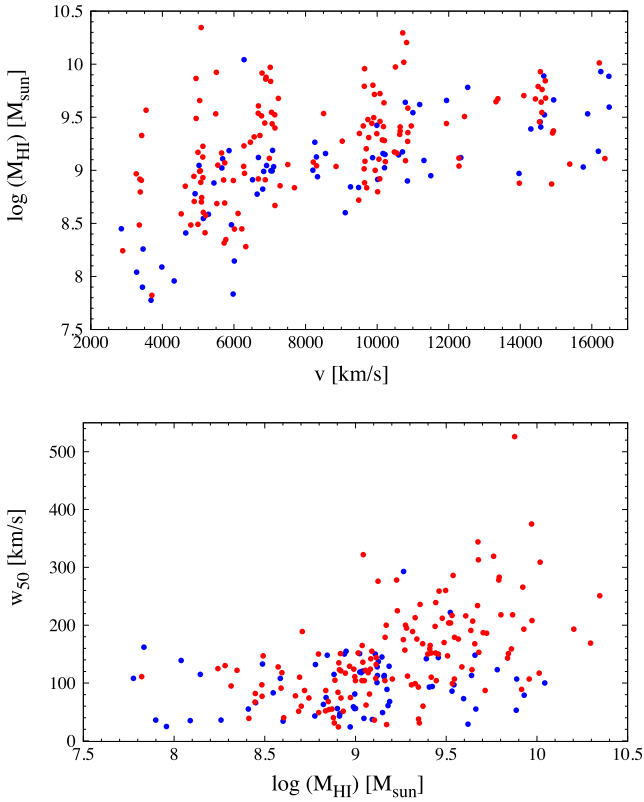


**Figure 7.** A comparison between global H I properties of detected galaxies with near-infrared counterparts (red) and without (blue). The top panel shows the total H I mass as a function of radial velocity. The bottom panel shows the  $w_{50}$  line width as a function of total H I mass.

Additionally, we also searched the *Wide-field Infrared Survey Explorer* (*WISE*; Wright 2010) images for counterparts, by inspecting the W1 (3.4  $\mu\text{m}$ ), W2 (4.6  $\mu\text{m}$ ) and W3 (12  $\mu\text{m}$ ) colour composite images. For this search we examined images 3 arcmin  $\times$  3 arcmin in size, specially constructed for the field using the method described in Jarrett et al. (2012). Only those galaxies closest to the H I position were considered and verified by eye as counterparts. In total 47 per cent of the galaxies detected in H I were found to have a *WISE* counterpart.

In a further step, we investigated H I properties that might have affected the recovery of a UKIDSS counterpart. They are displayed in Fig. 7 where we plot the total H I mass of all detected galaxies as a function of velocity and their  $w_{50}$  line width as a function of H I mass. Detections with near-infrared counterparts are shown in red and those without a counterpart in blue. We find relatively more counterparts for H I-massive  $\log(M_{\text{HI}}/M_{\odot}) = 9.5$  galaxies with large line widths ( $w_{50} > 150 \text{ km s}^{-1}$ ). We also note that most galaxies below  $\log(M_{\text{HI}}/M_{\odot}) = 8.4$  do not have identifiable near-infrared counterparts. These low H I-mass detections are usually gas-rich, low surface brightness galaxies and are not easily detectable in the near-infrared.

In Fig. 8 we overlay the spatial distribution of the H I detections on a  $K$ -band Galactic extinction ( $A_K$ ) map from the DIRBE/*IRAS*<sup>6</sup> data (Schlegel, Finkbeiner & Davis 1998; Schlafly & Finkbeiner 2011). Galaxies with near-infrared counterparts are indicated in red and those without in blue. The observed WSRT mosaic is outlined

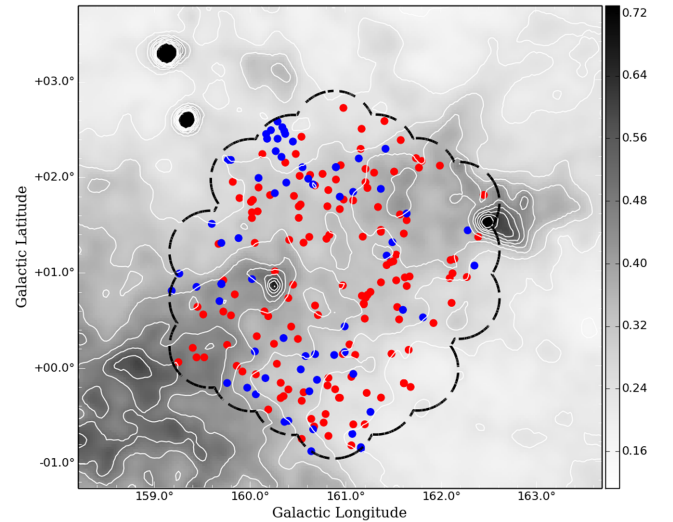


**Figure 8.** The spatial distribution of galaxies detected in H I. Galaxies with a near-infrared counterpart are shown in red, those without a counterpart in blue. They are superimposed on a DIRBE/*IRAS* map of  $A_K$  Galactic extinction values in the NIR  $K$  band, ranging from 0.16 to 0.72 mag as shown on the grey-scale bar. These correspond to  $A_B = 1.8$  to 8.0 mag, respectively in the  $B$  band optical.

by the black dashed contour. The plot indicates that finding a galaxy counterpart at  $\ell \approx 160^\circ$  behind the GP does not seem to depend on Galactic extinction. The small group of H I detections without a near-infrared counterpart in the top left of the plot is due to poor UKIDSS imaging in that area.

## 5 THE H I CATALOGUE AND ATLAS

### 5.1 The H I catalogue

The derived H I parameters of all detected galaxies are listed in tables presented in supplementary materials available online. The first table (Table A1) lists the resolved galaxies and the second table (Table A2) the marginally resolved galaxies (see Section 4.2 for details on how sources were divided into these two categories). The first 10 entries of each of these tables are shown in Tables 2 and 3 to illustrate their structure. The column entries of the 211 H I detections are as follows.

Column (1): galaxy designated identification based on the Right Ascension and Declination (J 2000.0) of the H I centroid.

Column (2) and (3): Galactic longitude and latitude in degrees.

Column (4): systemic velocity in the barycentric-standard of rest (BSR) defined by the central velocity in  $\text{km s}^{-1}$  of the global H I profile.

Column (5) and (6): observed H I profile line widths and their uncertainties (in  $\text{km s}^{-1}$ ) measured at 20 per cent and 50 per cent level of the H I profile peak flux, respectively, determined at a velocity resolution of  $16.5 \text{ km s}^{-1}$ .

Column (7): the integrated H I flux ( $S_{\text{int}}$ ) corrected for primary beam attenuation, in  $\text{Jy km s}^{-1}$ .

Column (8): luminosity distance  $D$  to the galaxy in Mpc derived from the systemic velocity measured in the BSR.

Column (9): the total H I mass in  $M_{\odot}$ .

Column (10): the H I radius measured at the  $1 M_{\odot} \text{ pc}^{-2}$  surface density level ( $R_{\text{HI}}$ ) in kpc, given for resolved sources only.

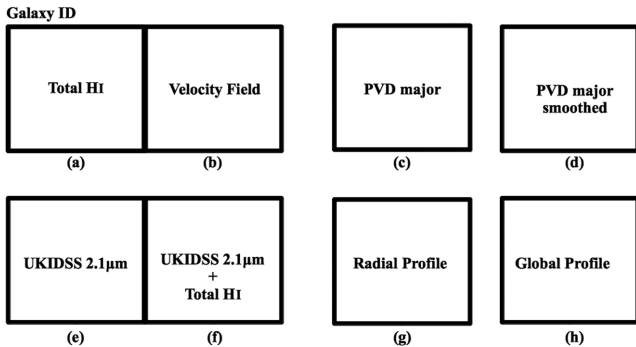
<sup>6</sup> <http://irsa.ipac.caltech.edu/applications/DUST/>

**Table 2.** A sample table showing the structure of the catalogue for resolved galaxy detections. The full table is available online.

ZoA	$\ell$	$b$	$v_{\text{rad}}$	$w_{20}$	$w_{50}$	$S_{\text{int}}$	$D$	$\log(M_{\text{H I}})$	$R_{\text{H I}}$	Counterpart
(1)	deg	deg	$\text{km s}^{-1}$	$\text{km s}^{-1}$	$\text{km s}^{-1}$	$\text{Jy km s}^{-1}$	Mpc	$M_{\odot}$	kpc	(11)
J044427.17+455116.7	159.25	0.06	5506 ± 04	285 ± 14	266 ± 09	5.68 ± 0.41	79	9.9	24.2	u –
J044521.10+454432.8	159.44	0.11	5134 ± 03	290 ± 07	278 ± 07	1.34 ± 0.10	73	9.2	12.4	u –
J044542.87+442101.0	160.54	–0.75	10717 ± 01	198 ± 04	169 ± 03	3.57 ± 0.10	153	10.3	33.5	u –
J044602.33+443426.8	160.40	–0.56	6281 ± 03	117 ± 10	100 ± 06	5.78 ± 0.45	90	10.0	31.0	– –
J044632.27+452152.2	159.86	0.02	9740 ± 02	226 ± 06	212 ± 08	0.66 ± 0.05	139	9.5	17.4	u w
J044644.10+442004.0	160.67	–0.62	5654 ± 05	194 ± 13	179 ± 13	0.94 ± 0.09	81	9.2	12.7	u w
J044644.74+444734.7	160.32	–0.32	5709 ± 03	156 ± 09	135 ± 10	0.51 ± 0.05	82	8.9	9.9	u –
J044700.10+442439.7	160.64	–0.54	10747 ± 02	330 ± 07	309 ± 05	1.86 ± 0.09	154	10.0	35.8	u w
J044706.91+453449.0	159.76	0.24	4994 ± 03	216 ± 08	200 ± 06	1.24 ± 0.06	71	9.2	14.0	u w
J044727.30+445342.4	160.32	–0.16	5523 ± 02	69 ± 06	51 ± 06	0.33 ± 0.03	79	8.7	7.9	u –

**Table 3.** A sample table for marginally resolved galaxy detections. The full table is available online.

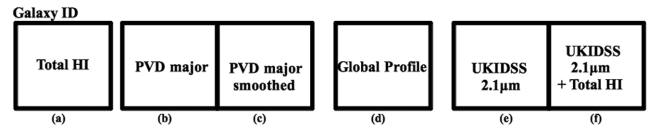
ZoA	$\ell$	$b$	$v_{\text{rad}}$	$w_{20}$	$w_{50}$	$S_{\text{int}}$	$D$	$\log(M_{\text{H I}})$	Counterpart
(1)	deg	deg	$\text{km s}^{-1}$	$\text{km s}^{-1}$	$\text{km s}^{-1}$	$\text{Jy km s}^{-1}$	Mpc	$M_{\odot}$	(10)
J044524.14+451924.3	159.76	–0.16	6830 ± 06	108 ± 18	59 ± 16	0.43 ± 0.07	98	9.0	– –
J044533.70+441127.9	160.64	–0.88	2852 ± 01	90 ± 02	66 ± 03	0.71 ± 0.05	41	8.4	– –
J044540.97+454045.8	159.52	0.11	9660 ± 02	153 ± 06	142 ± 08	0.27 ± 0.03	138	9.1	u –
J044541.51+455022.6	159.40	0.21	14584 ± 03	217 ± 09	123 ± 07	0.43 ± 0.05	208	9.6	u –
J044546.04+444901.5	160.19	–0.44	5134 ± 05	94 ± 34	51 ± 10	0.68 ± 0.09	73	8.9	u –
J044550.59+443552.5	160.36	–0.57	16249 ± 05	95 ± 13	79 ± 16	0.67 ± 0.10	232	9.9	– –
J044556.60+450741.4	159.97	–0.21	6803 ± 03	82 ± 14	63 ± 08	0.30 ± 0.04	97	8.8	– –
J044559.91+450104.1	160.06	–0.28	12528 ± 05	171 ± 10	123 ± 42	0.80 ± 0.13	179	9.8	– –
J044630.07+451655.0	159.92	–0.04	10229 ± 05	170 ± 12	124 ± 18	0.24 ± 0.04	146	9.1	u w

**Figure 9.** Schematics of the panel arrangement of the derived H I data products for resolved galaxies.

Column (11): indication of an infrared counterpart, found in either UKIDSS (u), *WISE* (w) or 2MASS (m).

## 5.2 The H I atlas

The H I data products described in Section 4 are presented here for all detected galaxies. They are shown in an H I atlas composed of two sections. The first section shows the resolved galaxies (one galaxy per page). The second provides maps of the marginally resolved galaxies (three per page). Schematics of the display panels are given in Figs 9 and 10, respectively. An example page of the resolved and marginally resolved cases is presented in Figs 11 and 12, respectively, the full atlas is available as supplementary material online. The panels presented in the respective atlases are as following.

**Figure 10.** Schematics of the panel arrangement of the derived H I data products for marginally resolved galaxies.

**Total H I map.** The total H I maps are presented at full angular resolution in panel (a) of Figs 9 and 10. The H I column density contour levels are at 1, 2, 4, 8, 16, 32... × 10<sup>20</sup> atoms cm<sup>–2</sup>. The FWHM beam size is indicated by the hatched ellipse. The dashed line indicates the direction of the morphological major axis determined as the position angle of the fitted two-dimensional Gaussian. The adopted H I centre position is indicated by a small white cross.

**Velocity fields.** In panel (b) of Fig. 9 the H I velocity fields are presented at an angular resolution of 30 arcsec (not shown for marginally resolved galaxies in Fig. 10). Pixels shown in grey-scales are where the radial velocity was measured. Lighter grey-scales and blue contours show the approaching side, darker and red contours the receding side of the rotating H I disc. The systemic velocity as derived from the global H I profile ( $v_{\text{sys}}$ ) is shown by the green contour. Contours are drawn from  $v_{\text{sys}}$  at intervals of 5, 10, 15, ..., 30, 35 km s<sup>–1</sup> depending on the width of the global H I profile. The dashed line indicates the adopted kinematic major axis and the white circle indicates the location of the adopted dynamical centre. The FWHM beam size is indicated by the hatched circle.

**Position velocity diagrams.** Shown in panels (c) and (d) of Fig. 9 and (b) and (c) of Fig. 10 are the major-axis PVDs at full angular resolution (23 arcsec and 16 arcsec). The panels show the PVD at a velocity resolution of 16.5 km s<sup>–1</sup> (left) and 66 km s<sup>–1</sup> (right),

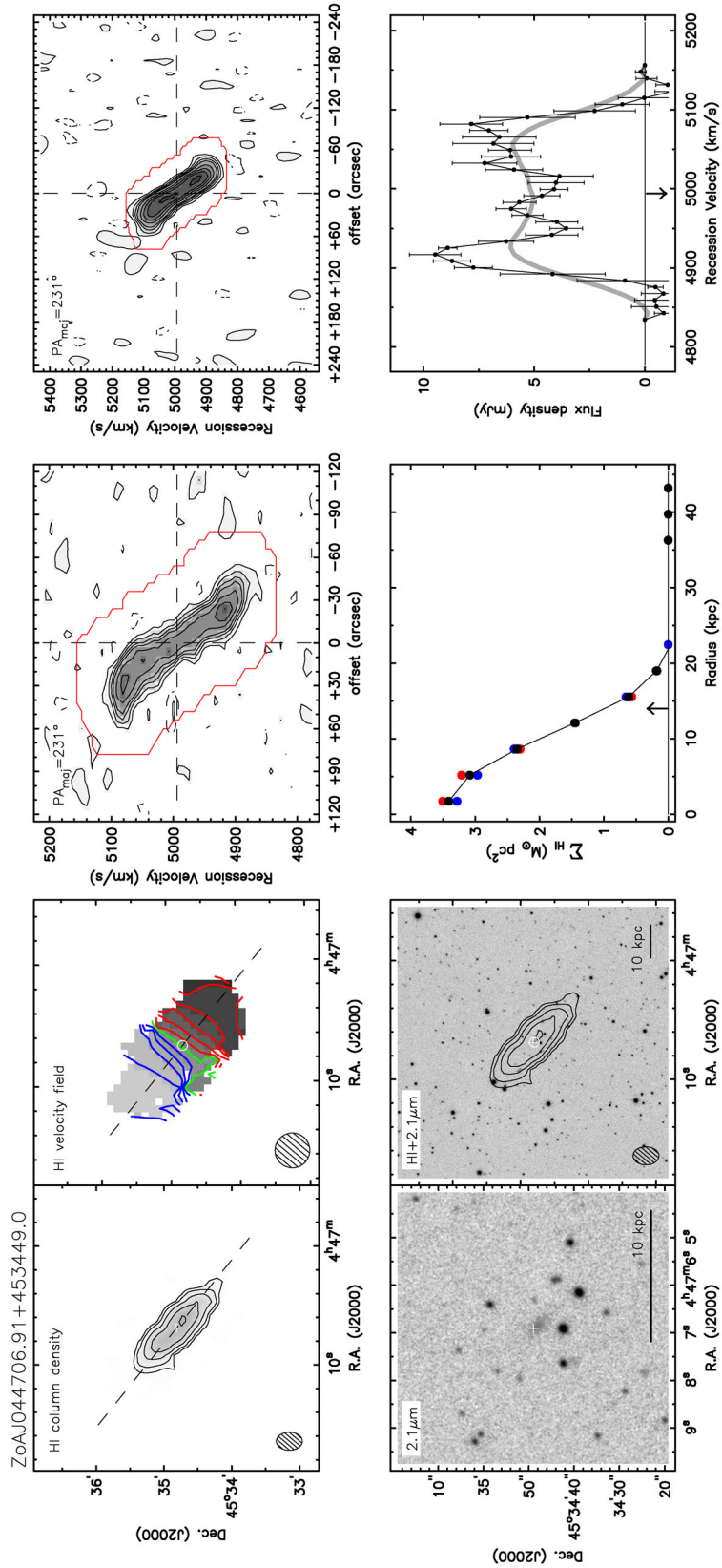


Figure 11. A sample atlas page for resolved sources.



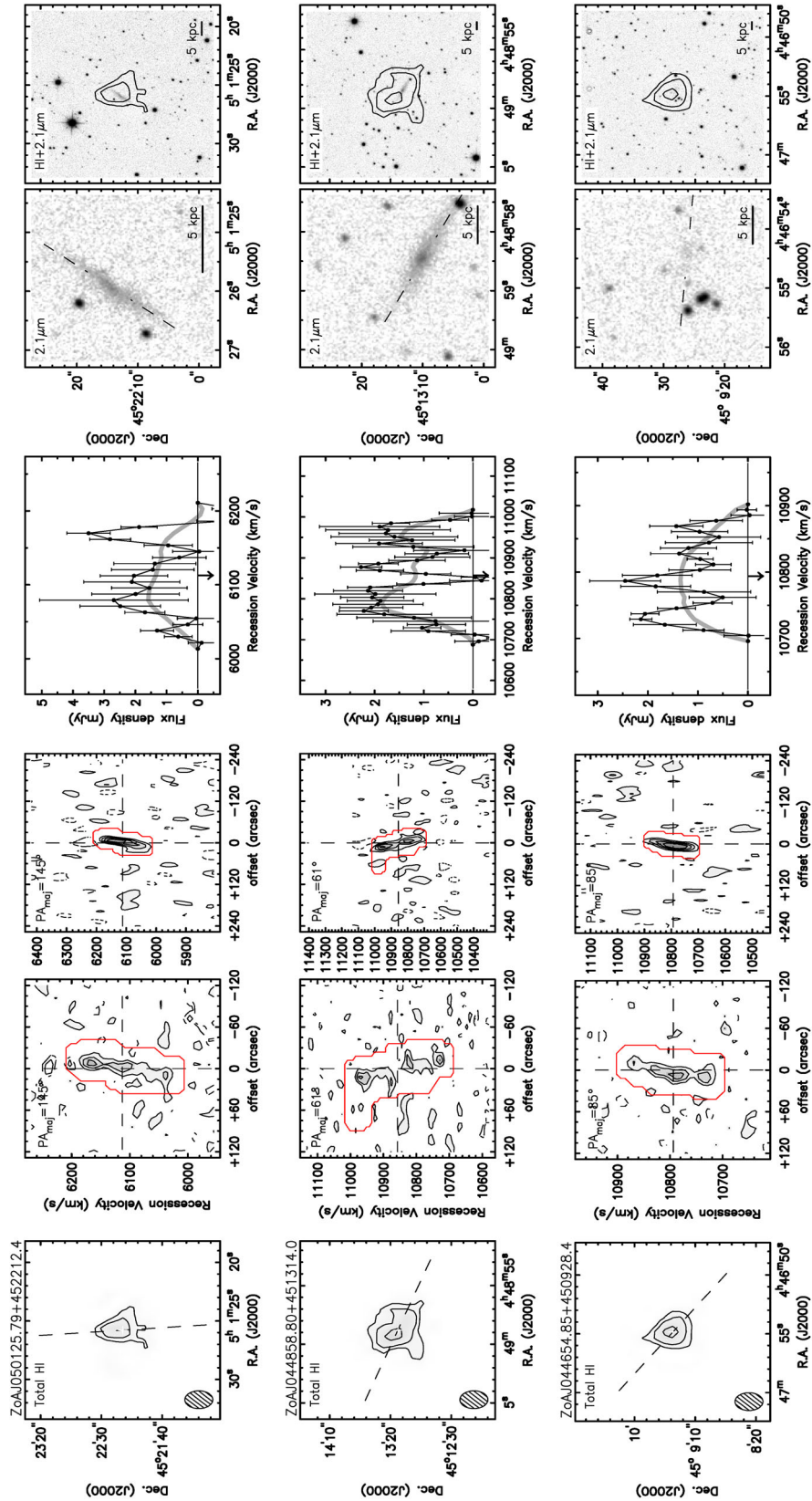


Figure 12. A sample atlas page for marginally resolved sources.

respectively. The position angle is indicated in the top left corner of each panel. The horizontal dashed line indicates the systemic velocity and the vertical dashed line the adopted centre of rotation. The red contour outlines the H I emission clean mask within which the integrated flux was determined. Contour levels are  $-3$  (dashed),  $-1.5$  (dashed),  $1.5$ ,  $3$ ,  $4.5$ ,  $6$ ,  $9$ ,  $12$ ,  $15$ ,  $20$ ,  $25$ ,  $30$  times the local rms noise level.

*Near-Infrared images.* Panels (e) of Figs 9 and 10, respectively show the  $1 \text{ arcmin} \times 1 \text{ arcmin}$  and  $0.5 \text{ arcmin} \times 0.5 \text{ arcmin}$ , near-infrared UKIDSS GPS K-band ( $2.1 \mu\text{m}$ ) images (Lawrence et al. 2007; Lucas et al. 2008). For cases where an UKIDSS image was unavailable due to imaging artefacts, a 2MASX Ks-band ( $2.1 \mu\text{m}$ ) image is shown instead. The white cross indicates the H I centre position. In panels (f) of Figs 9 and 10, we overlaid the contours of the total H I map on a  $2.5 \text{ arcmin} \times 2.5 \text{ arcmin}$  sized version of the near-infrared image, to show the extent of H I in comparison to the NIR component of the galaxy. For the resolved galaxies, the white cross and circle indicate the H I position and adopted dynamical centre, respectively. For the marginally resolved galaxies, the dashed line, if present, indicates the position angle of the identified near-infrared counterpart.

*Radial density profile.* The radial H I column density profiles, corrected for a face-on orientation, are shown only for the resolved galaxies in panel (g) of Fig. 9. The red and blue points indicate the receding and approaching side, respectively. The connected black points indicate the azimuthally averaged profile. The H I radius  $R_{\text{HI}}$  where the azimuthally averaged column density has dropped to  $1 \text{ M}_{\odot} \text{pc}^{-2}$  is indicated by the vertical arrow. No correction for beam-smearing has been applied.

*Global profile.* Figs 9 and 10, panels (d) and (h), show the global H I profiles. The connected black dots give the primary-beam corrected integrated H I flux density in each channel at a velocity resolution of  $16.5 \text{ km s}^{-1}$ . The grey thick line is the H I profile derived from cubes that have been smoothed to  $66 \text{ km s}^{-1}$ . Indicated errors are derived as described in Section 4. The vertical arrow points to the systemic velocity.

### 5.3 Previous H I detections

We cross-correlated our detections with H I detections reported in the literature. This was carried out using the NASA/IPAC Extragalactic Database (NED) and the Lyon/Meudon Extragalactic Database (HyperLeda; Paturel et al. 2003). Using positional and velocity information, both data bases were searched for galaxies previously detected in H I over our entire volume. We also made a comparison with the unpublished results of the NRT 2MASX H I follow-up survey (Kraan-Korteweg et al., in preparation). Three galaxies were found, all of which had been observed with the NRT. All three were also detected in our WSRT survey. It is not surprising that only three galaxies were found in these data bases, given the paucity of previous observations and detections over our WSRT survey area. The two galaxies with published H I data were initially identified in optical searches by Weinberger (1980) and subsequently observed in H I (Chamaraux et al. 1990; Paturel et al. 2003). The third galaxy was detected in the NRT 2MASX H I follow-up survey.

The H I parameters measured by them and those of our survey are given in Table 4. The respective values of velocity and line widths of all three galaxies are in good agreement. The integrated fluxes ( $S_{\text{int}}$ ) of ZoA J045747.05+460717.5 and its literature counterpart are also in good agreement. However, our WSRT integrated flux measurement of ZoA J045132.28+442922.2 is six times lower

**Table 4.** A comparison of H I profile parameters with literature values.

ZoA	$v$ km s <sup>-1</sup>	$w_{50}$ km s <sup>-1</sup>	$w_{20}$ km s <sup>-1</sup>	$S_{\text{int}}$ Jy km s <sup>-1</sup>
(1)	(2)	(3)	(4)	(5)
PGC 016173 (Wein 072) [1]	5201	255	323	6.70
J045132.28+442922.2	5129±4	276±11	305±11	1.06±0.07
Wein 069 [2]	5178	–	285	14.60
J045145.44+443610.2	5086±1	251±2	269±1	17.63±0.32
04574731+4607167 [3]	7199±9	370	408	4.27±0.56
J045747.05+460717.5	7013±1	375±3	393±3	3.96±0.11

[1] Paturel et al. 2003

[2] Chamaraux et al. 1990

[3] Kraan-Korteweg et al. (in preparation)

than that of PGC 016173 as measured by Paturel et al. (2003). To investigate this discrepancy, the relevant WSRT H I data cube was carefully examined by eye. No indication of any missed H I emission was found at that location. We then searched for a nearby, possibly confusing source within the large NRT beam ( $22 \text{ arcmin}$  FWHM in Declination). Its presence is indeed confirmed and illustrated in Fig. 13 which shows the H I column density map of the targeted galaxy in a larger field of view for the radial velocity range of  $4752\text{--}5576 \text{ km s}^{-1}$  together with the respective NRT beams. In this total H I map our WSRT H I detection cross-identified with PGC 016173 corresponds to the southernmost galaxy in this group. It is obvious that the NRT beam picked up excess H I flux from the nearby H I-bright galaxy Wein 069 at top left, with an integrated flux as measured with the WSRT of  $17.6 \text{ Jy km s}^{-1}$ , explaining the higher NRT flux measurement.

For the third detection in common, ZoA J045145.44+443610.2 or Wein 069, we measured a slightly higher total integrated flux than Chamaraux et al (1990). This galaxy is in fact the large easternmost source in Fig. 13. Its H I diameter is large ( $72.8 \text{ kpc}$ ), resulting in an incomplete flux measurement for the narrow NRT beam.

We cannot provide any further statistical comparison with the literature, given the fact that only three previous detections were cross-identified with our detections.

### 5.4 Completeness

The completeness of our catalogue is defined as the fraction of sources detected by the survey from an underlying sample distribution. As a first estimate for this paper we use the integrated flux to estimate the completeness based on an empirical approach. Our method is based on inserting artificial sources throughout the surveyed volume and determining the rate at which they are recovered with our source finding scheme.

The artificial galaxies were based on simulations by Obreschkow et al. (2009a) who for about  $3 \times 10^7$  galaxies evaluated the cosmic evolution of the atomic and molecular phases of the cold gas. Their simulations were based on the Semi-analytic Suite of SKA Simulated Skies (S<sup>2</sup>-SAX; De Lucia & Blaizot 2007) and are built on physical models applied to the semi-analytical model of evolving galaxies for the Millennium simulations (Springel et al. 2005). They cover a redshift range of  $z = 0\text{--}1.2$ , a sky area field of  $10 \text{ deg}^2$  and comprise galaxies with H I-peak flux  $\geq 1 \mu\text{Jy}$  (Obreschkow et al. 2009b).

For our survey volume the simulations predict H I properties for 1183 galaxies spanning H I masses and integrated fluxes ranging from  $\log(M_{\text{HI}}/M_{\odot}) = 6.05\text{--}10.26$  and  $S_{\text{int}} = 0.001\text{--}4.149 \text{ Jy km s}^{-1}$ ,

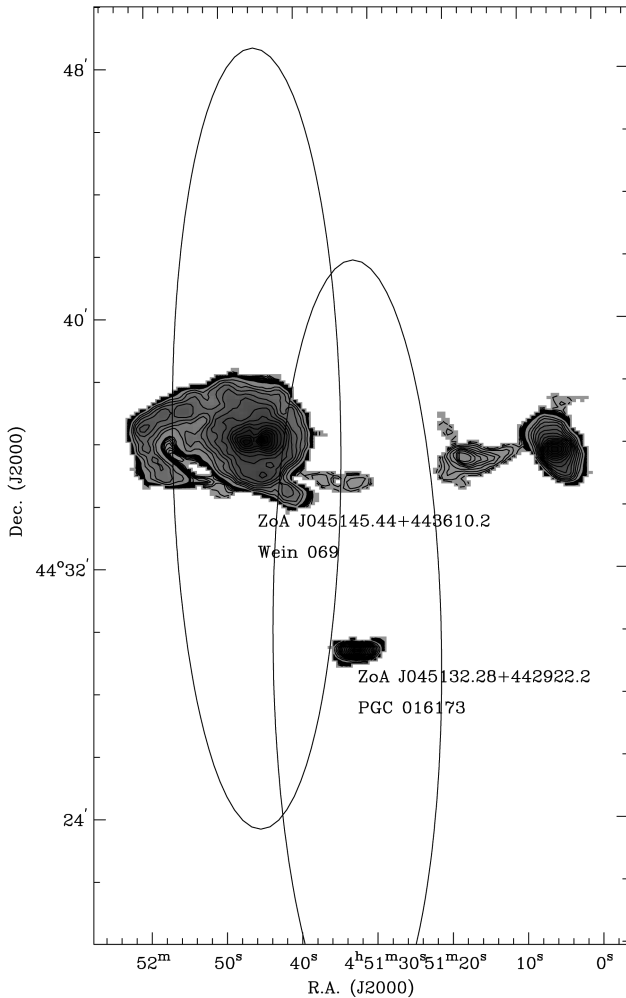


**Figure 13.** An illustration to show why our measured WSRT flux of ZoA J045132.28+442922.2 is six times lower than the NRT value reported by Patrel et al. (2003). The WSRT total H I maps of ZoA J045145.44+443610.2 (Wein 069, on the left) and ZoA J045132.28+442922.2 (PGC 016173, at the bottom) with the NRT FWHM beam sizes of the reported literature detections overlaid. The NRT detection of the latter is confused by the former, which is much stronger. In addition, we detected ZoA J045105.4+443544.0 at a similar recession velocity on the right.

respectively. The set of evaluated H I properties of each galaxy were used to build a detailed three-dimensional model of the spatial and spectral distribution of the H I line emission. All of the three-dimensional models were inserted in a single large synthetic cube matching our survey volume and the distribution of LSSs. This cube was then spatially smoothed to match the 23 arcsec  $\times$  16 arcsec beam of our WSRT observations. This final synthetic cube served as our noise-free sky model which was subsequently added to our observed data cube.

The data cube with the inserted artificial sources was then searched using the same procedure and detection criteria used to search for real galaxies as described in Section 3. No visual inspection of the artificial sources was done since their positions and redshifts were known a priori. The real sources were then removed from the list of detections such that only the detected artificial sources remained. A total of 101 artificial sources were recovered. The completeness for the whole WSRT survey was estimated by

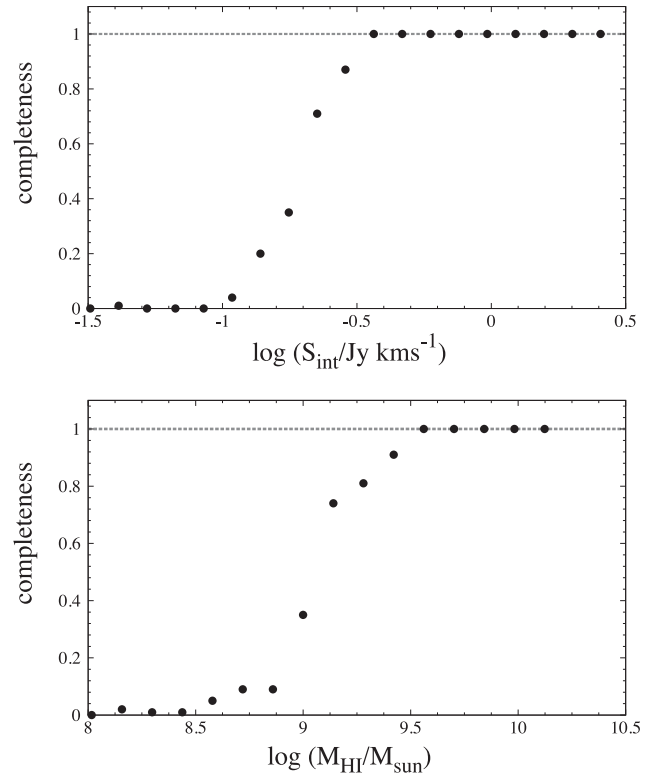


**Figure 14.** Completeness of the WSRT PP ZoA survey as function of the integrated H I line flux (top panel) and the H I mass (bottom panel). Points represent the fraction of artificial objects recovered in each bin. The grey dotted horizontal line represent where the survey is complete.

measuring the fraction of artificial sources recovered in given integrated flux and H I mass bins as represented Fig. 14.

From the detection rates of the simulated galaxies it follows that the WSRT PP ZoA survey is complete for objects with  $\log(S_{\text{int}}/\text{Jy km s}^{-1}) > -0.45$  ( $S_{\text{int}} = 0.35 \text{ Jy km s}^{-1}$ ). The minimum integrated flux of an object to be detected by the WSRT PP ZoA survey is  $\log(S_{\text{int}}/\text{Jy km s}^{-1}) > -0.98$  ( $S_{\text{int}} = 0.1 \text{ Jy km s}^{-1}$ ). From the bottom panel of Fig. 14 we show that our survey is complete for galaxies with H I masses of  $\log(M_{\text{HI}}/M_{\odot}) > 9.5$ .

We do however note that completeness is not just a measure of one parameter. A correction has to be made by integrating over another parameter such as the line width and peak flux as well as applying weighting to account for the relative source abundance in each parameter bin. In addition, given the depth of the survey, we expect the completeness to vary as a function of velocity. The completeness presented should therefore be regarded as a first approximation. In a forthcoming paper of this series we will provide a more robust verification and description.

## 6 THE DISTRIBUTION OF H I PROPERTIES OF DETECTED GALAXIES

To investigate the H I properties of the 211 detected galaxies, we plot the distributions of a number of their measured global H I parameters in histograms (see Fig. 15): their radial velocities,  $w_{50}$  line widths, integrated line fluxes and total H I masses.

We have visually identified four main overdensities along the line of sight by assessing their velocity distribution in combination with their spatial distribution. Since these features are located in the Auriga (Aur) constellation, we name them accordingly Aur 1

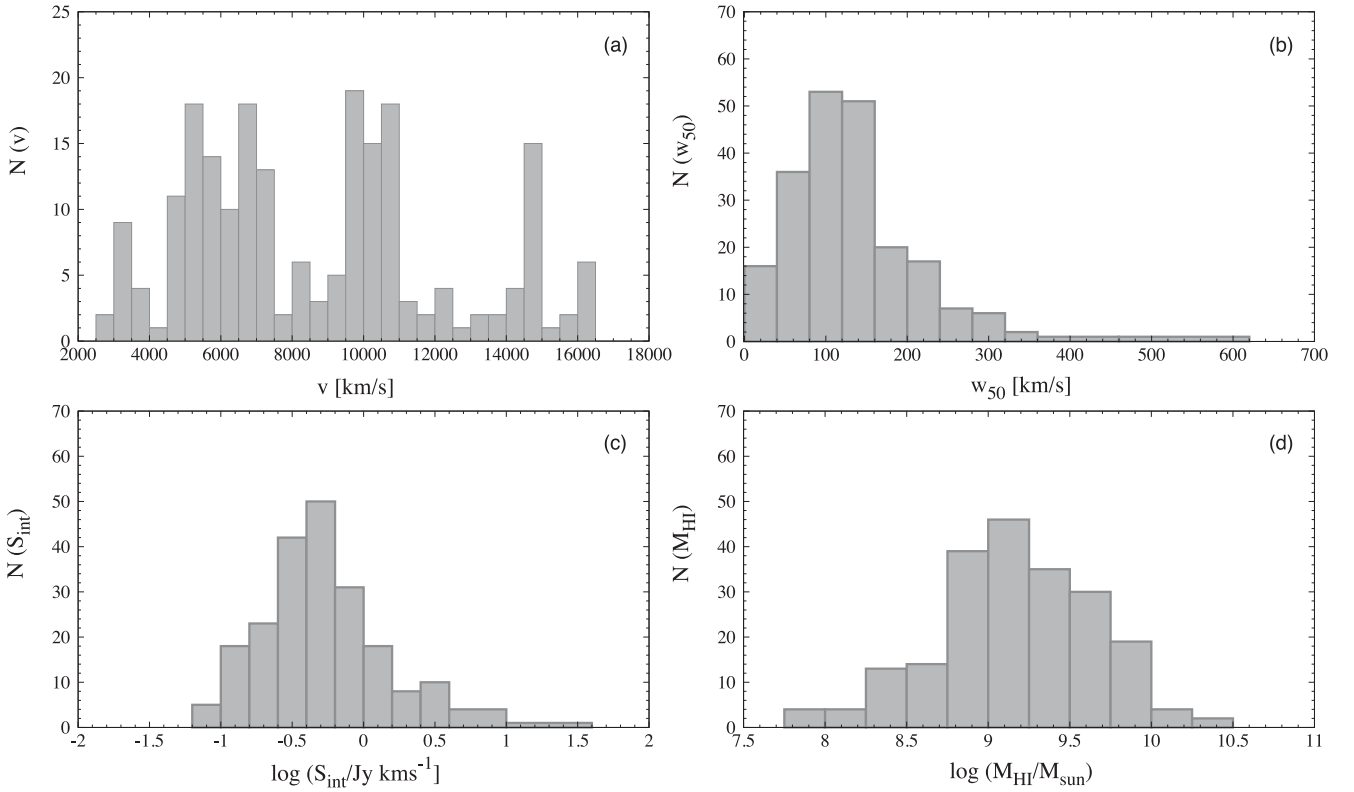


**Figure 15.** Distributions of selected H I parameters of the WSRT ZoA PP detected galaxies. Top left: radial velocity ( $v$ ). Top right: line width at the 50 per cent peak flux level ( $w_{50}$ ). Bottom left: logarithm of the integrated line flux ( $\log S_{\text{int}}/\text{Jy km s}^{-1}$ ). Bottom right: logarithm of the total H I mass.

to Aur 4. The nearest peak in redshift space is at  $\sim 3000 \text{ km s}^{-1}$  (Aur 1) and may be a galaxy group, whereas the most prominent and broadest overdensity extends over  $4500\text{--}7500 \text{ km s}^{-1}$  (Aur 2), i.e. at the approximate PPS redshift range. This is followed by a further distinctive peak at  $9500\text{--}11\,000 \text{ km s}^{-1}$  (Aur 3) and a narrower peak close to the high-end redshift range of our survey, at  $15\,000 \text{ km s}^{-1}$  (Aur 4). Of all the detections, 41 per cent and 34 per cent are associated with the two most prominent peaks Aur 2 and Aur 3, respectively. In between these peaks, regions nearly completely devoid of galaxies are evident, indicating a wide range of cosmic environments probed with this interferometric survey over a wide velocity range. Further details on these structures are given in Section 7.

In the  $w_{50}$  line widths histogram, the widths range from  $24\text{--}526 \text{ km s}^{-1}$ , but most of the galaxies have  $w_{50} < 225 \text{ km s}^{-1}$  and group around an average of  $132 \text{ km s}^{-1}$ . This is lower than the average  $w_{50}$  of  $186 \text{ km s}^{-1}$  of the  $\alpha.40$  catalogue of the Arcibo Legacy Fast ALFA survey (ALFALFA  $\alpha.40$ ; Haynes et al. 2011). This difference can be explained by the relatively large coverage ( $\sim 2800 \text{ deg}^2$ ) and lower sensitivity of  $2.2 \text{ mJy}$  of the ALFALFA survey, which leads to a higher average H I mass of  $\log(M_{\text{HI}}/M_{\odot}) = 9.5$  (see Fig. 16) and therefore a larger average line width (c.f., bottom panel of Fig. 7).

In the distribution of the integrated line fluxes, the average value is  $\log(S_{\text{int}}/\text{Jy km s}^{-1}) = -0.32$ , and the fluxes span the range from  $\log(S_{\text{int}}/\text{Jy km s}^{-1}) = -1.40$  to  $1.25$ , while the majority is restricted to a much tighter range of  $\log(S_{\text{int}}/\text{Jy km s}^{-1}) = 0.6$  to  $1.0$  ( $0.35 < S_{\text{int}} < 1.0 \text{ Jy km s}^{-1}$ ).

The H I mass distribution ranges from  $\log(M_{\text{HI}}/M_{\odot}) = 7.7$  to  $10.3$ . This is not excessively high compared to the most H I-massive

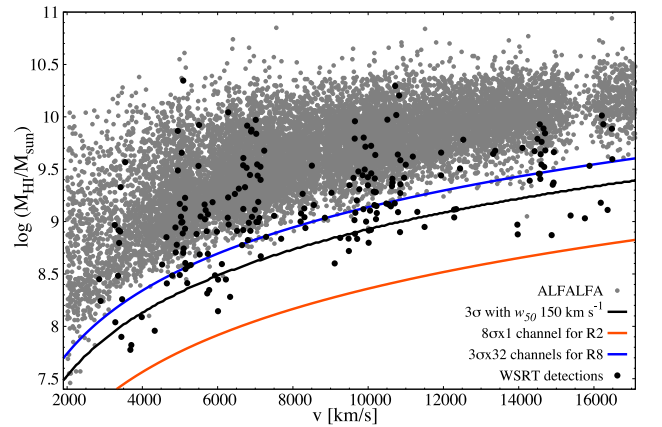


**Figure 16.** Logarithm of total H I masses of galaxies detected in our survey (black dots) and the ALFALFA survey (grey points) as a function of radial velocity. The black curve indicates the H I mass limit for the WSRT ZoA PP survey assuming a  $3\sigma$  detection with a  $150 \text{ km s}^{-1}$  line width. In orange we show the H I mass limit of a detection at  $8\sigma \times 1$  channel for a velocity resolution of  $16.5 \text{ km s}^{-1}$  (R2). The blue curve shows the H I mass limit of a detection at  $3\sigma \times 32$  channels for a velocity resolution of  $66 \text{ km s}^{-1}$  (R8).

galaxies known, which can reach  $10.8$  (e.g. Cluver et al. 2010). This is due to the relatively small volume surveyed. The overall galaxy distribution has a mean H I mass of  $\log(M_{\text{HI}}/M_{\odot}) = 9.1$ , which is below that of ALFALFA of  $\log(M_{\text{HI}}/M_{\odot}) = 9.5$ . There is a non-negligible fraction of lower H I mass detections.

To assess where galaxies with different H I masses are found in redshift, we plot in Fig. 16 our H I masses as function of radial



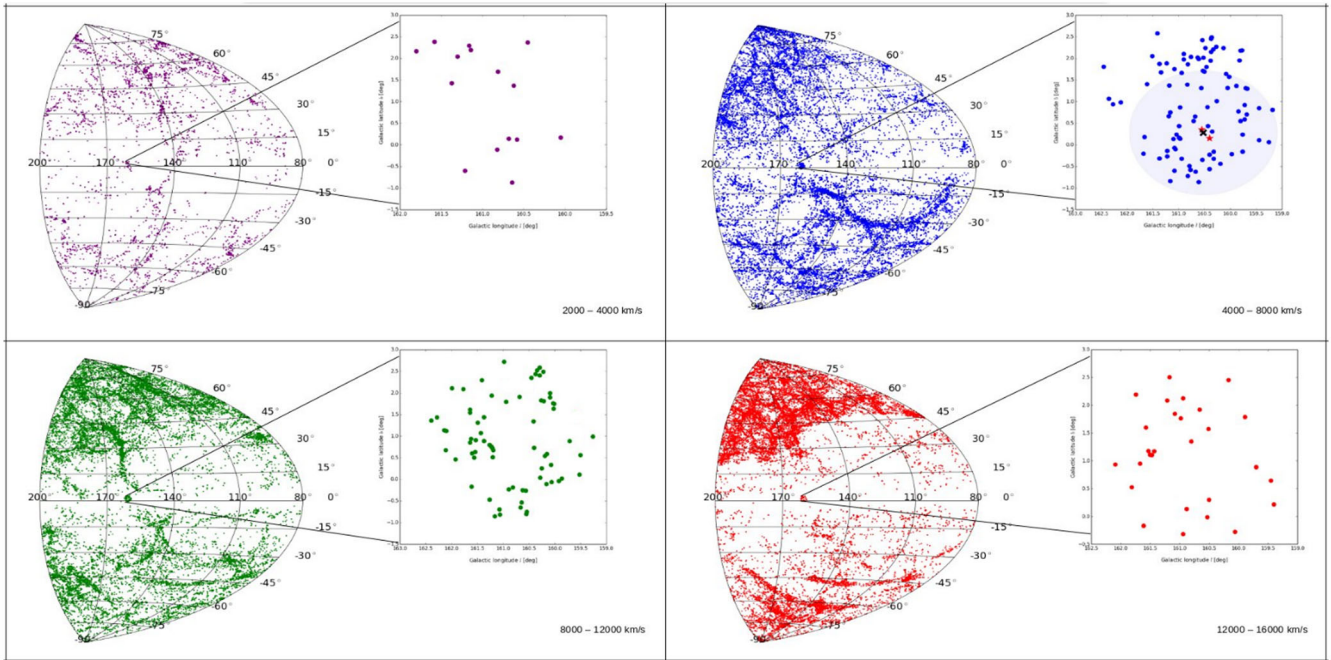


**Figure 17.** Aitoff projections of the sky-distribution in Galactic coordinates for  $80^\circ < \ell < 200^\circ$  and  $-90^\circ < b < 90^\circ$ . Galaxies with known redshifts from the literature and the 2MRS are shown as dots. The images at the top right corner of each panel show a zoomed-in on the spatial distributions of galaxies detected by the WSRT ZoA PP survey and point to their location within the context of the LSSs they reside in. The galaxy sky distributions are separated into four radial velocity bins. Top left:  $2000\text{--}4000\text{ km s}^{-1}$  (Aur 1), top right:  $4000\text{--}8000\text{ km s}^{-1}$  (Aur 2), the light shaded area indicates 1 Abell radius of 85 arcmin at this distance, centred on the 3C 129 cluster indicated by the black cross. Positions of the radio galaxies are indicated by red stars. Bottom left:  $8000\text{--}12000\text{ km s}^{-1}$  (Aur 3) and bottom right:  $12000\text{--}16000\text{ km s}^{-1}$  (Aur 4).

velocity. The black curve shows the predicted H I mass detection limit of our survey at the  $3\sigma$  noise level for a galaxy with  $w_{50}$  of  $150\text{ km s}^{-1}$ . The two prominent peaks indicating clustering at about  $6000$  and  $10000\text{ km s}^{-1}$  are once again evident. Galaxies found at these distances have H I masses ranging from  $\log(M_{\text{H I}}/M_{\odot}) = 7.8\text{--}10.3$  and  $8.6\text{--}10.3$ , respectively. To gauge how the H I masses of our detections compare to those from other surveys, we also show H I masses from the ALFALFA survey in grey. In general we find objects with lower H I masses at all velocities which is consistent with the lower rms noise of  $\sim 0.4\text{ mJy}$  of our WSRT survey compared to the  $2.2\text{ mJy}$  of ALFALFA.

## 7 LSSs CROSSING THE ZoA

Our survey does not have a large enough areal coverage to explore the angular distribution of the LSSs at the different redshift peaks. However, it is deep enough to explore prominent LSSs that cross the GP in radial velocity space. We have found galaxies over the full radial velocity range of  $cz = 2400\text{--}16600\text{ km s}^{-1}$ . Their velocity distribution is not homogenous, which is not unexpected given that we targeted a cluster and its environment at about  $6000\text{ km s}^{-1}$ . Interestingly, behind the targeted cluster we also find evidence for either a clustering, a cross-section of a filament or a wall.

To explore the unveiled structures in the context of known LSS, we extracted galaxies with known redshifts from the literature (mainly the 2MRS) in the surroundings of our WSRT survey area. The 2MRS survey is homogenous and ‘all-sky’ down to Galactic latitude  $|b| = 5^\circ$ . However, it should be noted that it is NIR-selected and therefore favours early-type galaxies as opposed to the late-types typically detected in H I samples. Given the lack of other deep all-sky galaxy imaging or H I surveys, this remains the best

data set to compare our results with and to study the connectivity of known LSSs across this area of the ZoA. It should be noted though that the peak sensitivity in redshift space of the 2MRS lies at about  $12000\text{ km s}^{-1}$  and that it is very sparsely sampled above  $15000\text{ km s}^{-1}$ .

In Fig. 17, the detected H I galaxies are plotted together with adjacent galaxies with known redshifts in an equal-area Aitoff sky projection for the Galactic coordinate range  $80^\circ < \ell < 200^\circ$  and  $-90^\circ < b < 90^\circ$ , for four different radial velocity ranges. To clarify the effect of the new H I detections in the small WSRT region ( $9.6\text{ deg}^2$ ), we provide a zoomed-in plot next to the large area map for each of the redshift intervals. The different panels or colours represent the four overdensity peaks identified in Fig. 15, namely in purple (Aur 1;  $2000\text{--}4000\text{ km s}^{-1}$ ), blue (Aur 2;  $4000\text{--}8000\text{ km s}^{-1}$ ), green (Aur 3;  $8000\text{--}12000\text{ km s}^{-1}$ ) and red (Aur 4;  $12000\text{--}16000\text{ km s}^{-1}$ ). The picture of the new ZoA crossing features becomes even clearer when assessing their positions in a redshift wedge (Fig. 18) which displays the Galactic longitude range of  $155^\circ\text{--}165^\circ$  for the latitude range  $-30^\circ < b < 30^\circ$ . The blue dashed lines outline our surveyed volume.

New features include a small number of nearby galaxies (Aur 1). The most prominent feature is Aur 2, around  $6000\text{ km s}^{-1}$ , an overdensity associated with the 3C 129 X-ray cluster and the two strong radio sources, 3C 129 and 3C 129.1 (see Section 1). Further out in the  $8000\text{--}12000\text{ km s}^{-1}$  (green) redshift range a new striking feature peaking at  $10000\text{ km s}^{-1}$  dominates. Additionally, we are seeing hints of the edge of another structure, C31, identified by Erdođdu et al. (2006), at  $14000\text{--}16000\text{ km s}^{-1}$ . However, the number of detections at these higher radial velocities is relatively low because it lies close to the high-velocity limit of our survey where the H I mass sensitivity is reduced. In addition, the 2MRS

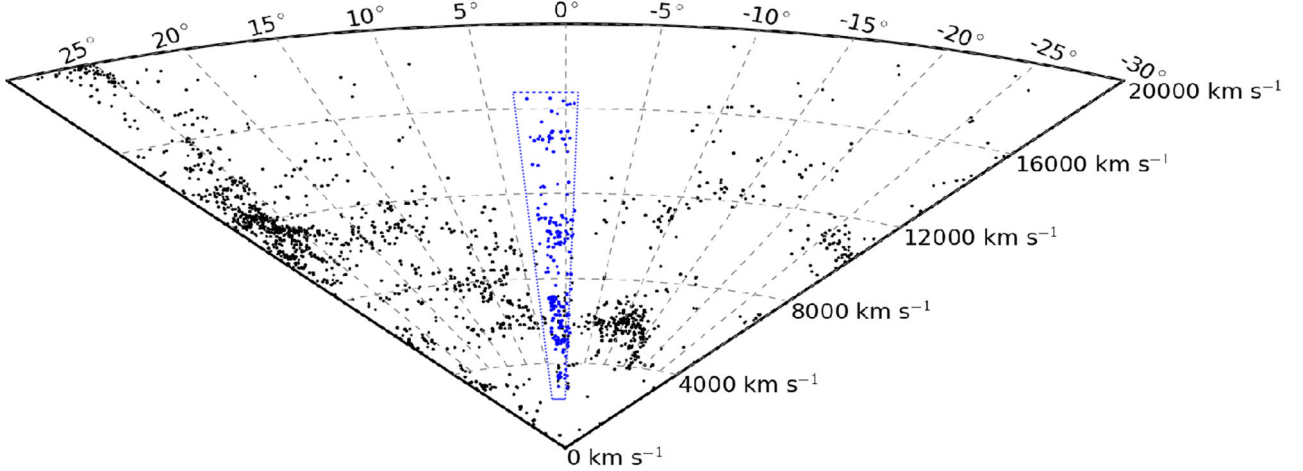


**Figure 18.** Redshift wedge diagram for  $155^\circ < \ell < 165^\circ$  and  $-30^\circ < b < 30^\circ$ . Galaxies with known redshifts from the literature and the 2MRS out to  $cz \approx 20\,000 \text{ km s}^{-1}$  are plotted in black. The WSRT PP ZoA survey region (at about  $-1^\circ < b < 4^\circ$ ) is outlined by blue dashed lines and new detections are represented by blue dots.

has lost most of its sensitivity at  $\geq 15\,000 \text{ km s}^{-1}$ . Nevertheless, it clearly marks a high-density region, as demonstrated in Figs 16 and 18. For these reasons, concrete conclusions regarding this most distant galaxy density peak, cannot be drawn at present.

The newly identified structures already pointed out in Section 6 are discussed in detail in the following subsections, starting with the two most prominent structures, Aur 2 and Aur 3, followed by a short overview of the minor structures Aur 1 and Aur 4.

### The PPS connection

The PPS is the most noticeable linear feature in the Northern sky around  $cz \approx 6000 \text{ km s}^{-1}$  (e.g. Giovanelli & Haynes 1985; Giovanelli, Haynes & Chincarini 1986; Haynes et al. 1988; Wegner, Haynes & Giovanelli 1993). The main ridge of the PPS is a linear filamentary structure of about 45 Mpc in length (Seeberger, Huchtmeier & Weinberger 1994), bounded in  $\ell$  between  $80^\circ$  and  $180^\circ$ . It comprises a rich chain of Abell clusters such as ACO 262, ACO 347 and ACO 426 (Gregory, Thompson & Tift 1981; Wegner et al. 1993).

In the top right panel of Fig. 17 the PPS can be traced from  $\ell, b \approx 80^\circ, 15^\circ$ , entering the ZoA at  $\ell \approx 90^\circ$  and emerging on the other side at  $\ell, b \approx 90^\circ, -5^\circ$ , the connection of which was confirmed to extend across the Milky Way by the NRT ZoA survey (Kraan-Korteweg et al., in preparation). The filament bends all the way to the South of the ZoA at  $\ell, b \approx 120^\circ, -30^\circ$ , where it connects to ACO 2634 ( $\ell, b \approx 103^\circ, -33^\circ$ ) and ACO 2666 ( $\ell, b \approx 107^\circ, -33^\circ$ ) at  $cz \approx 8000 \text{ km s}^{-1}$  (Merighi et al. 1986). It then bends at a slight angle, vanishing into the ZoA at  $\ell \approx 160^\circ$  and reappears aligned with the main ridge at  $cz \approx 6000 \text{ km s}^{-1}$ .

It is based on this observation that Focardi et al. (1984) proposed an extension of the PPS across the ZoA towards a clump of galaxies associated with ACO 569 (see also Focardi, Marano & Vettolani 1986). This suggestion stemmed from a ‘conglomerate of galaxies’ hinted at in Weinberger (1980) at  $\ell \approx 160^\circ$ , where Spinrad (1975) had measured radial velocities of the two radio galaxies mentioned in Section 1. The lack of data in the obscured ZoA prompted further extensive studies (Focardi et al. 1984, 1986; Chamaraux et al. 1990; Lu & Freudling 1995; Pantoja et al. 1997; Saurer, Seeberger & Weinberger 1997) ultimately confirming this link. It is clear now that

our new observations not only substantiate this continuity, but also prove that this connection incorporates yet another major cluster that forms part of the PPS.

The H I detections in our survey are associated with the 3C 129 X-ray cluster with a mass of  $M_X = 5 \times 10^{14} M_\odot$ , centred at  $\ell, b \approx 160^\circ.52, 0^\circ.28$  (Leahy & Yin 2000) which, when added to the overall Perseus-Pisces chain, makes the PPS one of the largest known structures in the local Universe. In fact, Chamaraux et al. (1990) showed that its dimension could be as large as 150–300 Mpc, with the addition of other clusters in the South of the ZoA. Moreover, it has been postulated in the past that the PPS could be as densely populated as, or even more, than the Great Attractor (Saunders et al. 1991; Strauss & Willick 1995; Hudson et al. 1997). Adding this new mass overdensity to the overall mass of the PPS might lead to significant infall motions of galaxies in its immediate surroundings. A complete and detailed dynamical examination of this galaxy cluster, including flows associated with the structure, is one of the questions that will be addressed in a forthcoming paper of this series.

### Behind the PPS

The background of the PPS (see the bottom left panel of Fig. 17) comprises galaxies in the velocity range  $8000\text{--}12\,000 \text{ km s}^{-1}$ . In this range, the most dominant filamentary structure is evident. The Aur 3 overdensity of galaxies is part of this structure, which can be traced from  $\ell, b \approx 170^\circ, 45^\circ$  to the North of the ZoA, traversing the ZoA at  $\ell \approx 160^\circ$ , emerging from the ZoA at  $\ell \approx 150^\circ$  to the South. It continues towards a cluster dominated by early type galaxies at  $\ell, b, cz \approx 143^\circ, -22^\circ, 10\,720 \text{ km s}^{-1}$  (J7; Wegner et al. 1996). It then bends at a slight angle and diffuses into a sheet of galaxies at  $\ell \gtrsim 143^\circ, b \lesssim 40^\circ$ . The new H I detections in the ZoA at  $\ell \approx 160^\circ$  are not associated with any known cluster. However, they coincide with a structure, CID 15 predicted by Erdođdu et al. (2006) in the 2MRS reconstructed density and velocity maps.

### Additional ZoA Structures

Both the top left ( $cz \approx 2000\text{--}4000 \text{ km s}^{-1}$ ) and bottom right ( $cz \approx 12\,000\text{--}16\,000 \text{ km s}^{-1}$ ) panels of Fig. 17 indicate hints of galaxy overdensities. The nearer one, Aur 1, is too widely spread over the

survey area to associate the detections with any LSS in the vicinity. The more distant one, Aur 4 at the far edge of the survey volume does coincide with another structure, C31, predicted by Erdoğan et al. (2006) (see their fig. 10) at  $cz \approx 14\,000\text{--}16\,000\text{ km s}^{-1}$ , although the actual galaxy map (Fig. 17) does not give a clear hint of a connection to this feature. It seems to emerge from below the GP and ends in the ZoA without continuing into the Northern Galactic hemisphere. There is not enough data for a quantitative analysis.

## 8 SUMMARY

We have conducted a blind 21cm H I-line imaging survey with the WSRT of the area where the PPS crosses the ZoA, centred at  $\ell, b \approx 160^\circ, 0.5^\circ$ . The survey comprises an effective area of  $\sim 9.6\text{ deg}^2$  observed at an angular resolution of  $23\text{ arcsec} \times 16\text{ arcsec}$  and a velocity resolution of  $16.5\text{ km s}^{-1}$  with an average rms noise level of  $0.36\text{ mJy beam}^{-1}$  over the radial velocity range of  $cz = 2400\text{--}16\,600\text{ km s}^{-1}$ . We detected 211 H I sources, of which only three had previously been detected in H I. We have presented the results as a data catalogue with derived H I-parameters and as an H I atlas with total H I maps and velocity fields, major axis PVDs, global line profiles and overlays with near-infrared images. A total of 80 sources were resolved by the WSRT. We found near-infrared counterparts for 130 (62 per cent) of our detections from UKIDSS and 100 (47 per cent) mid-infrared counterparts from WISE. In cases where a UKIDSS image could not be found due to imaging artefacts we searched a 2MASS image at comparable wavelength to the UKIDSS K-band. The radial velocity distribution of our H I detections shows four overdensities crossing the GP. The most prominent is a connection between the PPS above and below the ZoA and associated with the 3C 129 X-ray cluster. The new detections support previous claims that the PPS filament extends to the cluster A 569. Of particular interest is another ZoA structure behind the PPS at a radial velocity of  $10\,000\text{ km s}^{-1}$ . While predicted previously, it has now been detected for the first time. It seems to belong to a prominent large scale filament at  $10\,000\text{ km s}^{-1}$  which comprises one other known cluster, J7, residing just below the ZoA. The data presented here provide input for an upcoming detailed analysis of the 3C 129 cluster and the other overdensities detected, to be presented in forthcoming papers in this series.

## ACKNOWLEDGEMENTS

MR acknowledges financial support from the Ubbo Emmius Fund of the University of Groningen. MR, RKK, ACS, TJ and EE acknowledge the research support provided by the South African National Research Foundation. Authors from South Africa and the Netherlands of this collaboration all benefitted tremendously from collaborative exchanges support by the NRF/NWO bilateral agreement for Astronomy and Astronomy Enabling Technologies. MV acknowledges financial support from the DAGAL network for the People Programme (Marie Curie Actions) of the European Unions Seventh Framework Programme FP7/2007-2013/ under REA grant agreement number PITNGA-2011-289313. MV acknowledges support by a Vici grant from the Innovational Research Incentives Scheme of the Netherlands Organisation for Scientific Research (NWO). MV also acknowledges the Leids Kerkhoven Bosscha Fonds (LKBF) for travel support. We would also like to thank K. Said, B. Frank, R. Juraszek, B. Koribalski, P. Serra, L. Flöer, L. Staveley-Smith and I. Wong for their various contributions to the project. The Westerbork Synthesis Radio Telescope is operated by the ASTRON

(Netherlands Institute for Radio Astronomy) with support from the Netherlands Foundation for Scientific Research (NWO).

This publication makes use of data products from the Two Micron All Sky Survey, which is a joint project of the University of Massachusetts and the Infrared Processing and Analysis Center/California Institute of Technology, funded by the National Aeronautics and Space Administration and the National Science Foundation.

This research has also made use of the UKIRT Infrared Deep Sky Survey data base.

This publication also makes use of data products from the WISE, which is a joint project of the University of California, Los Angeles, and the Jet Propulsion Laboratory/California Institute of Technology, funded by the National Aeronautics and Space Administration.

This research also makes use of the HyperLEDA data base (<http://leda.univ-lyon1.fr>) and the NASA/IPAC Extragalactic Database (NED) which is operated by the Jet Propulsion Laboratory, California Institute of Technology, under contract with the National Aeronautics and Space Administration

## REFERENCES

- Bilicki M., Jarrett T. H., Peacock J. A., Cluver M. E., Steward L., 2014, *ApJS*, 210, 9
- Branchini E., Plionis M., 1996, *ApJ*, 460, 569
- Casali M. et al., 2007, *A&A*, 467, 777
- Chamaraux P., Cayatte V., Balkowski C., Fontanelli P., 1990, *A&A*, 229, 340
- Cluver M. E., Jarrett T. H., Kraan-Korteweg R. C., Koribalski B. S., Appleton P. N., Melbourne J., Emonts B., Woudt P. A., 2010, *ApJ*, 725, 1550
- Colless M. et al., 2001, *MNRAS*, 328, 1039
- de Blok W. J. G., 2011, *Proc. IAU Symp.*, 277, 96
- De Lucia G., Blaizot J., 2007, *MNRAS*, 375, 2
- Donley J. L. et al., 2005, *AJ*, 129, 220
- Dressler A., Faber S. M., Burstein D., Davies R. L., Lynden-Bell D., Terlevich R. J., Wegner G., 1987, *ApJ*, 313, L37
- Duffy A. R., Meyer M. J., Staveley-Smith L., Bernyk M., Croton D. J., Koribalski B. S., Gerstmann D., Westerlund S., 2012, *MNRAS*, 426, 3385
- Ebeling H., Edge A. C., Bohringer H., Allen S. W., Crawford C. S., Fabian A. C., Voges W., Huchra J. P., 1998, *MNRAS*, 301, 881
- Eisenstein D. J. et al., 2011, *AJ*, 142, 72
- Erdoğan P. et al., 2006, *MNRAS*, 373, 45
- Fixsen D. J., Kashlinsky A., 2011, *ApJ*, 734, 61
- Focardi P., Marano B., Vettolani G., 1984, *A&A*, 136, 178
- Focardi P., Marano B., Vettolani G., 1986, *A&A*, 161, 217
- Giovanelli R., Haynes M. P., 1985, *AJ*, 90, 2445
- Giovanelli R., Haynes M. P., Chincarini G. L., 1986, *ApJ*, 300, 77
- Gregory S. A., Thompson L. A., Tift W. G., 1981, *ApJ*, 243, 411
- Greisen E. W., 1990, in Longo G., Sedmak G., eds, *Acquisition, Processing and Archiving of Astronomical Images*. Finito di stampare da Officine Grafiche Liguori, Napoli, p. 125
- Hambly N. C. et al., 2008, *MNRAS*, 384, 637
- Haynes M. P., Magri C., Giovanelli R., Starosta B. M., 1988, *AJ*, 95, 607
- Haynes M. P. et al., 2011, *AJ*, 142, 170
- Henning P. A. et al., 2010, *AJ*, 139, 2130
- Hewett P. C., Warren S. J., Leggett S. K., Hodgkin S. T., 2006, *MNRAS*, 367, 454
- Huchra J. P. et al., 2012, *ApJS*, 199, 26
- Hudson M. J., 1993, *MNRAS*, 265, 43
- Hudson M. J., Lucey J. R., Smith R. J., Steel J., 1997, *MNRAS*, 291, 488
- Jarrett T., 2004, *PASA*, 21, 396
- Jarrett T. H., Chester T., Cutri R., Schneider S., Skrutskie M., Huchra J. P., 2000, *AJ*, 119, 2498
- Jarrett T. H. et al., 2012, *AJ*, 144, 68



- Jones D. H. et al., 2004, MNRAS, 355, 747  
 Kerr F. J., Henning P. A., 1987, ApJ, 320, L99  
 Kocevski D. D., Ebeling H., 2006, ApJ, 645, 1043  
 Kraan-Korteweg R. C., 2005, Rev. Mod. Astron., 18, 48  
 Kraan-Korteweg R. C., Lahav O., 2000, A&AR, 10, 211  
 Kraan-Korteweg R. C., Loan A. J., Burton W. B., Lahav O., Ferguson H. C., Henning P. A., Lynden-Bell D., 1994, Nature, 372, 77  
 Lavaux G., Hudson M. J., 2011, MNRAS, 416, 2840  
 Lavaux G., Tully R. B., Mohayaee R., Colombi S., 2010, ApJ, 709, 483  
 Lawrence A. et al., 2007, MNRAS, 379, 1599  
 Leahy D. A., Yin D., 2000, MNRAS, 313, 617  
 Loeb A., Narayan R., 2008, MNRAS, 386, 2221  
 Lu N. Y., Freudling W., 1995, ApJ, 449, 527  
 Lucas P. W. et al., 2008, MNRAS, 391, 136  
 McIntyre T. P., Henning P. A., Minchin R. F., Momjian E., Butcher Z., 2015, AJ, 150, 28  
 Masters K. L., Springob C. M., Huchra J. P., 2008, AJ, 135, 1738  
 Merighi R., Focardi P., Marano B., Vettolani G., 1986, A&A, 160, 398  
 Obreschkow D., Croton D., De Lucia G., Khochfar S., Rawlings S., 2009a, ApJ, 698, 1467  
 Obreschkow D., Klöckner H.-R., Heywood I., Levrier F., Rawlings S., 2009b, ApJ, 703, 1890  
 Oosterloo T., Verheijen M., van Cappellen W., ISKAF2010 Science Meeting The Latest on Apertif. 2010, p. 43  
 Pantoja C. A., Altschuler D. R., Giovanardi C., Giovanelli R., 1997, AJ, 113, 905  
 Paturel G., Theureau G., Bottinelli L., Gouguenheim L., Coudreau-Durand N., Hallet N., Petit C., 2003, A&A, 412, 57  
 Plionis M., Kolokotronis V., 1998, ApJ, 500, 1  
 Ramatsoku M., Kraan-Korteweg R., Schröder A., van Driel W., 2014, in van Rensburg J. J., ed., Proc. SAIP2012: the 57th Annual Conf. of the South African Inst. Phys., p. 368  
 Rowan-Robinson M. et al., 1990, MNRAS, 247, 1  
 Saunders W., Frenk C., Rowan-Robinson M., Lawrence A., Efstathiou G., 1991, Nature, 349, 32  
 Saurer W., Seeberger R., Weinberger R., 1997, A&AS, 126, 247  
 Schlafly E. F., Finkbeiner D. P., 2011, ApJ, 737, 103  
 Schlegel D. J., Finkbeiner D. P., Davis M., 1998, ApJ, 500, 525  
 Seeberger R., Huchtmeier W. K., Weinberger R., 1994, A&A, 286, 17  
 Spinrad H., 1975, ApJ, 199, L1  
 Springel V. et al., 2005, Nature, 435, 629  
 Stark A. A., Gammie C. F., Wilson R. W., Bally J., Linke R. A., Heiles C., Hurwitz M., 1992, ApJS, 79, 77  
 Staveley-Smith L., Kraan-Korteweg R. C., Schröder A. C., Henning P. A., Koribalski B. S., Stewart I. M., Heald G., 2016, AJ, 151, 52  
 Strauss M. A., Willick J. A., 1995, Phys. Rep., 261, 271  
 Truemper J., 1982, Adv. Space Res., 2, 241  
 van der Hulst J. M., Terlouw J. P., Begeman K. G., Zwitser W., Roelfsema P. R., 1992, in Worrall D. M., Biemesderfer C., Barnes J., eds, ASP Conf. Ser. Vol. 25, Astronomical Data Analysis Software and Systems I. Astron. Soc. Pac., San Francisco, p. 131  
 van Driel W., Schneider S. E., Kraan-Korteweg R. C., Monnier Ragaigine D., 2009, A&A, 505, 29  
 van Moorsel G., Kemball A., Greisen E., 1996, in Jacoby G. H., Barnes J., eds, ASP Conf. Ser. Vol. 101, Astronomical Data Analysis Software and Systems V. Astron. Soc. Pac., San Francisco, p. 37  
 Verheijen M. A. W., Oosterloo T. A., van Cappellen W. A., Bakker L., Ivashina M. V., van der Hulst J. M., 2008, in Minchin R., Momjian E., eds, AIP Conf. Ser. Vol. 1035, The Evolution of Galaxies Through the Neutral Hydrogen Window. Am Inst. of Phys., Maryland, p. 265  
 Wegner G., Haynes M. P., Giovanelli R., 1993, AJ, 105, 1251  
 Wegner G., Colless M., Baggle G., Davies R. L., Bertschinger E., Burstein D., McMahan R. K., Jr, Saglia R. P., 1996, ApJS, 106, 1  
 Weinberger R., 1980, A&AS, 40, 123

## SUPPORTING INFORMATION

Additional Supporting Information may be found in the online version of this article:

### Supplementary material\_tables.pdf

(<http://www.mnras.oxfordjournals.org/lookup/suppl/doi:10.1093/mnras/stw968/-/DC1>).

Please note: Oxford University Press is not responsible for the content or functionality of any supporting materials supplied by the authors. Any queries (other than missing material) should be directed to the corresponding author for the article.

This paper has been typeset from a  $\text{\TeX}/\text{\LaTeX}$  file prepared by the author.